

Influence of the North American Dipole on the Atlantic Warm Pool

Jinghua Chao

Chengdu University of Information Technology

Guangzhou Fan

Chengdu University of Information Technology

Ruiqiang Ding

Beijing Normal University

Quanjia Zhong (✉ zqj@lasg.iap.ac.cn)

Institute of Atmospheric Physics Chinese Academy of Sciences <https://orcid.org/0000-0002-6774-3146>

Zhenchao Wang

Chengdu University of Information Technology

Research Article

Keywords: Atlantic warm pool, North American dipole, North Atlantic Oscillation

Posted Date: May 28th, 2021

DOI: <https://doi.org/10.21203/rs.3.rs-545050/v1>

License:   This work is licensed under a Creative Commons Attribution 4.0 International License.

[Read Full License](#)

1 **Influence of the North American dipole on the Atlantic Warm Pool**

2 Jinghua Chao¹, Guangzhou Fan¹, Ruiqiang Ding², Quanjia Zhong^{*3} and Zhenchao
3 Wang¹

4

5 *¹School of Atmospheric Sciences, Chengdu University of Information Technology,*
6 *Chengdu 610225, China*

7 *²State Key Laboratory of Earth Surface Processes and Resource Ecology, Beijing*
8 *Normal University, Beijing 100875, China*

9 *³State Key Laboratory of Numerical Modeling for Atmospheric Sciences and*
10 *Geophysical Fluid Dynamics (LASG), Institute of Atmospheric Physics, Chinese*
11 *Academy of Sciences, Beijing 100029, China*

12

13 *(submitted to **Climate Dynamics**)*

14 *May 20, 2021*

15

16 *Corresponding author:*

17 Dr. Quanjia Zhong

18 State Key Laboratory of Numerical Modeling for Atmospheric Sciences and
19 Geophysical Fluid Dynamics (LASG), Institute of Atmospheric Physics, Chinese
20 Academy of Sciences, Beijing 100029, China

21 Email: zqj@lasg.iap.ac.cn

22

23

24

Abstract

25
26 The Atlantic warm pool (AWP) of water having a temperature above 28.5°C
27 encompasses the Gulf of Mexico, the Caribbean, and the western tropical North Atlantic,
28 influencing the regional and global climate. Much of the AWP interannual variability
29 has been thought to be an outcome of external remote forcing by climate variability
30 outside the tropical Atlantic, such as the El Niño-Southern Oscillation (ENSO) or the
31 North Atlantic Oscillation (NAO). This study indicates that the North American dipole
32 (NAD), exemplified by a north-south seesaw in sea level pressure anomalies over the
33 western tropical North Atlantic and northeastern North America, may provide another
34 integral remote forcing source to influence the AWP. Both observational and model data
35 prove that a strong positive (negative) phase of the winter NAD tends to inhibit (favor)
36 the development of AWP in its area and depth in subsequent months. As opposed to the
37 NAO, the NAD plays a more pivotal role in influencing the AWP due to its effectiveness
38 in forcing the TNA SST variability, which means that AWP variability may be more of
39 a lagging response to NAD atmospheric forcing than a lagging response to NAO
40 atmospheric forcing. Additional analysis indicates that the winter NAD-like
41 atmospheric signal may be stored in the following AWP, thus markedly influencing the
42 TNA precipitation and air temperature in summer. It is speculated that the AWP may
43 act as a bridge linking winter NAD to the following summer precipitation and air
44 temperature in the TNA region.

45 **Keywords:** Atlantic warm pool; North American dipole; North Atlantic Oscillation

46 **1. Introduction**

47 The Atlantic warm pool (AWP) of water warmer than 28.5°C comprises the
48 western tropical North Atlantic (TNA), the Gulf of Mexico, and the Caribbean (Wang
49 and Enfield 2001; Curtis 2013; Misra et al. 2016). The AWP appears in the boreal late
50 spring and reaches its maximum size in late summer (Czaja et al. 2002). The western
51 Pacific warm pool (Webster and Lukas 1992) straddles the equator whereas the AWP is
52 located entirely north of the equator (Wang and Enfield 2003).

53 As a source of heat and moisture for global atmospheric circulation, the AWP
54 exerts a notable influence on the regional and global climate (Wang and Lee 2008;
55 Wang et al. 2008a; Durán-Quesada et al. 2010; Drumond et al. 2011; Liu et al. 2015).
56 For instance, rainfall in eastern South America, Central America, and the Caribbean Sea
57 from August-October are closely linked to the AWP size (Wang et al. 2006).
58 Furthermore, many studies have also indicated that the AWP can affect the formation
59 and development of Atlantic hurricanes by prompting vertical wind shear changes and
60 moist static instability (Wang and Lee 2007; Wang et al. 2011).

61 The AWP exhibits a colossal interannual variability in its area and intensity (Misra
62 et al. 2013). Much of this variability is thought to be a consequence of remote forcing
63 by climate variabilities outside the tropical Atlantic, such as the ENSO (Covey and
64 Hastenrath 1978; Curtis and Hastenrath 1995; Enfield 1996; Nobre and Shukla 1996;
65 Giannini et al. 2000) and the North Atlantic Oscillation (NAO; Giannini et al. 2001;
66 Mo and Häkkinen 2001). Past studies have made mention that both the wintertime

67 ENSO and NAO events can be instrumental in driving TNA SST anomalies during
68 spring through their impact on latent heat exchange at the ocean surface and
69 subsequently cause the size of AWP to fluctuate the following summer (Enfield and
70 Mayer 1997; Liu et al. 2012). Enfield et al. (2006) investigated that the El Niño event
71 in the previous winter can result in an extraordinary summer AWP averaging about
72 twice the climatological annual size through an atmospheric bridge. Furthermore, they
73 also emphasized that the interannual fluctuations of the NAO may encroach with the
74 atmospheric bridge forcing from ENSO during the winter and, in turn, influence the
75 formation of large AWP in the following summer and fall.

76 The TNA SST plays an essential role in developing subsequent AWP, and the
77 positive SST anomalies in the TNA region are conducive to the generation of a large
78 AWP (Wang and Enfield 2003; Wang et al. 2008b). Previous studies mainly focused on
79 how remote forcing such as winter ENSO and NAO affects the AWP in the following
80 summer through their impact on spring TNA SST anomalies. Numerous recent findings
81 indicated a meridional dipole of sea level pressure (SLP) anomalies over northeastern
82 North America and the western tropical North Atlantic, the so-called North American
83 dipole (NAD; Ding et al. 2017, 2019). Both winter NAD and NAO present a dipole
84 characteristic of SLP anomalies in the North Atlantic but nevertheless carry significant
85 differences. The NAD is prone to force the SST anomalies in the TNA region more
86 effectively than the NAO, considering that the center of SLP anomalies related with the
87 NAD is further west and south as opposed to the NAO (Zhou et al. 2019). Owing to the
88 closer link of NAD with the TNA SST anomalies than NAO, it is speculated that the

89 winter NAD may also affect subsequent AWP development, which is likely a precursor
90 to the anomalous size of AWP.

91 The influence of NAD-like atmospheric variability on AWP size will be analyzed
92 in this study. The remainder of this paper is arranged as follows: Section 2 introduces
93 the datasets and analytical methods. The correlation between the NAD and the AWP
94 variability in both observations and numerical simulations are presented in section 3.
95 Section 4 consists of a summary of our main findings and provides a discussion.

96 **2 Data and methods**

97 **2.1 Observational Data Sets**

98 The Hadley Centre SST data set version 1 (HadISST1) was employed for the SST
99 analysis (Rayner et al. 2003). The precipitation field was extracted from the NOAA
100 Climate Prediction Center (CPC) Merged Analysis of Precipitation (CMAP) dataset
101 (Xie and Arkin 1997). Monthly atmospheric circulation data including winds, SLP,
102 specific humidity, velocity potential, and air temperature employed in this study were
103 procured from the National Centers for Environmental Prediction-National Center for
104 Atmospheric Research (NCEP-NCAR) reanalysis version I (Kalnay et al. 1996). All
105 datasets range from the years 1979 to 2019. The long-term linear trend and seasonal
106 cycle were considered obsolete and removed from all variables analyzed in this study.

107 **2.2 Model Data Sets**

108 To evaluate whether the effect of winter NAD on the following AWP can be

109 reproduced in the current coupled model, the monthly outputs of 25 coupled
110 atmosphere-ocean models participated in the Coupled Model Intercomparison Project,
111 Phase 6 (CMIP6) from preindustrial control (pi-Control) experiments were used in this
112 paper (Eyring et al. 2016). The variables analyzed from the CMIP6 models included:
113 SST, SLP, horizontal winds, precipitation, air temperature, and specific humidity. The
114 SST variable output by the CMIP6 was converted to a horizontal resolution of $1^\circ \times 1^\circ$.
115 In contrast, the other variables' production is converted to a horizontal resolution of 2.5°
116 $\times 2.5^\circ$, which concurs with the resolution of the observed data and aids the calculation
117 of the overall average. To circumvent the initial adjustment period caused by the
118 model's spin-up process, only the simulations run from the past century have been
119 analyzed in this paper.

120 2.3 Numerical experiment

121 The coupled model used in this study is the Flexible Global Ocean Atmosphere–
122 Land System model grid-point version 2 (FGOALS-g2) developed at State Key
123 Laboratory of Numerical Modeling for Atmospheric Sciences and Geophysical Fluid
124 Dynamics (LASG), Institute of Atmospheric Physics (IAP), Chinese Academy of
125 Sciences (Li et al. 2013). The four components of FGOALS-g2 include the atmospheric
126 component (Grid-point Atmospheric Model of IAP LASG version 2, GAMIL2); the
127 oceanic model (LASG IAP climate system ocean model version 2, LICOM2); the sea-
128 ice component (Community Ice Code, CICE4-LASG), improved the performance of
129 CICE4.0, and the introduced Community Land Model (CLM3) from the National

130 Center for Atmospheric Research (NCAR).

131 To further interpret the NAD's effect on the following AWP development, the
132 control and assimilation experiments were conducted. The difference between the
133 above two experiments is to assimilate the NAD-related winds (U, V) and air
134 temperature (T) anomalies at 1000hPa, 925hPa, and 850hPa in the western tropical
135 North Atlantic and northeastern North America, which arises from regressions of the
136 DJFM U, V and T anomalies onto the concurrent NADI (Fig. 2). The control experiment
137 is a historical run driven by external forcing observed from 1979 to 2018. Another
138 experiment assimilated the NAD-related U, V, and T anomalies imposed on the
139 climatological U, V, and T. The initialization is cycled at 40 years from 1979 to 2018
140 with a one-month assimilation windows. The past 25 years' output was applied to the
141 composite analysis to minimize the possible internal impact.

142 2.4 Indices

143 As per Ding et al. (2017), the NAD index (NADI) used here is defined as the
144 difference of normalized (i.e., subtracting the mean and then dividing by the standard
145 deviation) SLP anomalies between the southern (90° – 60° W, 10° – 30° N) and northern
146 (75° – 45° W, 55° – 70° N) poles (southern minus northern pole) after linearly excluding
147 the effect of the ENSO. The NAO index (NAOI) used in this study is defined as the
148 difference in the normalized SLP zonally averaged over the North Atlantic sector from
149 80° W to 30° E between 35° N and 65° N (Li and Wang 2003). According to Zhou et al.
150 (2019), the maximum seasonal variance between NAD and NAO ranged from

151 December to March (DJFM). Therefore, our research is based on the four-month
152 average DJFM NADI and NAOI. Figure 1b depicts the interannual time series of the
153 DJFM-averaged NADI (blue line) and NAOI (red line) for 1979–2018, where their
154 correlation was calculated at 0.49, which means that the variability of NAD is
155 independent of the NAO, confirming the findings of previous work.

156 According to Wang and Enfield (2003), two types of AWP indices have been
157 employed in this study. One is the AWP area index (AWPAI), the area within the 28.5°C
158 isotherms at the AWP region's sea surface. The other being the index of the depth
159 enclosed by the 28.5°C isotherms in the AWP region (referred to as the AWP depth
160 index, AWPDI).

161 2.5 Methods

162 This paper employs statistical methods, including composite analysis, correlation
163 analysis, and linear regression. The statistical significance is based on a two-tailed
164 Student's *t*-test, where the effective number (N^*) of degrees of freedom is calculated as
165 follows by Bretherton et al. (1999):

$$166 \quad N^* \approx N \frac{1-R_x R_y}{1+R_x R_y}, \quad (1)$$

167 where N is the sample size, and R_x , R_y represents the lag-one autocorrelations of
168 two-time series x and y , respectively.

169 **3. Results**

170 **3.1 Establishing the NAD-AWP Relationship**

171 To investigate the probable link between NAD and AWP, the lead-lag correlation
172 of the winter NADI (red line) with 3-month-averaged AWPDI for 1979–
173 2018 is illustrated in Figure 3. The peak correlation between NADI and AWPDI
174 ($R=-0.62$; significant at the 99 % confidence level) occurs during the months of May
175 to July (MJJ), lagging the NAD peak during winter by about five months. For the AWP
176 depth index, similar significant values (at the 99% level) began to appear during April–
177 June (AMJ), peak ($R=-0.60$) during MJJ, and also lingered to the following fall.
178 Moreover, Figure 4 details the correlation of the AWPDI during MJJ with
179 the SLP anomalies in the previous winter (DJFM-averaged). It is observed that the AWP
180 is closely linked to the pre-winter NAD-like dipole of SLP anomalies over the North
181 Atlantic (compared with the Fig. 1a).

182 The comparison of the composite analysis in the seasonal evolution of AWP area
183 between strongly positive and negative NAD events was subsequently carried out
184 (Table 1). It is defined as a strongly positive (negative) event of the NAD when the
185 winter NAD index is greater (less) than one positive (negative) standard deviation. As
186 depicted in Figure 5d, when the winter NAD is in its strong negative phase (blue line),
187 the AWP has developed in the Caribbean region during the months of April to June
188 (AMJ). Thereupon, the eastern edge of this AWP rushes eastward to TNA in the MJJ
189 and June–August (JJA) (Fig. 5f, d), provoking a twofold to a threefold increase in area

190 than the climatic state (Figs. 5b, c). Contrarily, the strong positive phase of the winter
191 NAD tends to inhibit the subsequent AWP development (see also in Figs. 5d–f; red line).
192 The above discussions analyze changes in the area of AWP, but a similar composite
193 analysis about changes in the depth of the AWP is also shown in Figure 6. The same
194 conclusion can be drawn that the strong positive (negative) phase of the winter NAD
195 tends to inhibit (favor) the development of AWP in its depth in subsequent months.

196 A similar lead/lag correlation of the winter NAOI (yellow line) with 3-month-
197 averaged AWPDI is also carried out in Figure 3b, but also contained weak
198 correlations. The previous winter NAO had little effect on the following area (refer to
199 Fig. 5) and depth (not shown) of AWP. This result indicates that, the NAD plays a more
200 pivotal role in influencing the AWP due to its efficiency at forcing the TNA SST
201 variability in contrast with the NAO. This shows that AWP variability is possibly more
202 of a lagging response to NAD atmospheric forcing rather than a lagging response to
203 NAO atmospheric forcing. Although the observational analysis above indicated a close
204 link between the NAD and AWP, it is limited by the relatively few NAD events. Further
205 investigations employing more extended datasets from the CMIP6 models support the
206 results of the observed data.

207 3.2 Possible mechanisms

208 3.2.1 Observational results

209 So far, the results have established a relationship between variability of the NAD

210 and AWP at seasonal time scales. To provide probable physical explanations for the
211 connection between the NAD and AWP, the evolutions of SST and surface winds
212 anomalies related with the winter NAD were subsequently analyzed. Figure 7 illustrates
213 the concurrent and lagged correlation maps of the DJFM-averaged NADI with the 3-
214 month averaged SST and surface winds anomalies for December–February (DJF),
215 March–May (MAM), May–July (MJJ), and July–September (JAS). The green box
216 denotes the extent of the AWP.

217 During winter (the DJF season, Fig. 7a), a tripole-like SST anomaly pattern
218 associated with the NAD is detected over the North Atlantic. Simultaneously, the SLP
219 anomalies related to the NAD are accompanied by surface winds anomalies, which can
220 force significant positive SST anomalies in the Gulf of Mexico and western North
221 Atlantic north of about 20°N and negative SST anomalies in the TNA through changes
222 in the latent heat flux recorded by Ding et al. (2017). Thereupon, the TNA SST cooling
223 reaches its maximum during spring (the MAM season, Fig. 7b) and perdure through the
224 following MJJ (Fig. 7c) and JAS (Fig. 7d) due to the wind–evaporation–SST (WES)
225 feedback (Xie and Philander 1994), expanding from the Caribbean to the Gulf of
226 Mexico. Given that the AWP is adjacent to the TNA, the remote forcing of NAD acts
227 on the AWP in a similar way as on the TNA: changes in surface winds provoke changes
228 of latent heat flux that subsequently generate AWP SST anomalies.

229 3.2.2 Numerical experiment results

230 To further interpret the NAD's effect on the following AWP development, the

231 control and assimilation experiments were conducted by the FGOALS-g2 model. The
232 composite differences in the seasonal evolutions of SST and surface winds anomalies
233 between the assimilation and control experiments are illustrated in Figure 8. The fact
234 that the NAD-related surface winds anomalies in the TNA can force negative SST
235 anomalies in the TNA via changes in the latent heat flux during winter and spring is
236 thoroughly understood (Figs. 8a, b). Thereafter, the TNA SST cooling persists through
237 the following MJJ and JAS (Figs. 8c, d), which may inhibit the following AWP's
238 eastward expansion. However, the TNA's negative SST during that time does not
239 exceed the 90% confidence level. These results from coupled model experiments are
240 almost concordant with those described in the observational data (Fig. 7) and further,
241 substantiate the winter NAD influences on the ensuing AWP development.

242 The above results indicate that the NAD-induced SST anomalies in TNA regions
243 play a crucial role in developing succeeding anomalous AWP size. The analyses further
244 prove the impact of the TNA SST on AWP size. In conclusion, the underlying physical
245 process of the influence of NAD-induced TNA SST on AWP is concordant with the
246 mechanism proposed by Enfield et al. (2006) to explain manifestations of anomalous
247 AWP's. However, the emphasis laid in this study is on the connection between the NAD
248 and AWP. Our analysis shows that the NAD has a vital role in the commencement of a
249 large AWP event.

250 3.3 Model Simulations

251 To evaluate whether the effect of winter NAD on subsequent AWP can be

252 reproduced in the current coupled model, we analyzed the monthly outputs of 25
253 coupled atmosphere-ocean models participated in CMIP6 (Table 2).

254 The models' abilities in simulating the NAD were assessed to evaluate the link
255 between the NAD and the AWP in models. Figure 9 illustrates that the spatial pattern
256 of DJFM-averaged NADI correlated with the concurrent SLP anomalies derived from
257 observation and the 25 CMIP6 models' simulations. All the models can replicate a
258 distinct dipole comprising of a low over northeastern North America and a high over
259 the western tropical North Atlantic, which is the signature feature of NAD. For the
260 locations of NAD centers, a majority of simulated magnitudes of NAD negative centers
261 have a northward displacement when compared to the observation. Furthermore, most
262 models can give an accurate representation of the NAD positive centers, though several
263 (EC-Earth3, MIROC6, MPI-ESM-1-2-HAM, MPI-ESM1-2-HR, and MRI-ESM2-0)
264 simulating this as extending too far off to the east. Henceforth, a Taylor diagram (Taylor,
265 2001) was employed to quantitatively measure the difference between model
266 simulations and observations and make inherent comparisons among the different
267 models (Fig. 10). Two-thirds of the pattern correlation coefficients between the
268 modeled and observed interannual NAD pattern were evaluated at more than 0.70,
269 indicating that the CMIP6 models generally mimic the NAD pattern. More than half of
270 the ratios of the standard deviations between modeled and observed NAD patterns are
271 valued to be less than 1.0, which confirms that most CMIP6 models underestimate the
272 NAD pattern. Concisely, HadGEM3-GC31-LL and FOGOALS-f3-L perform best at
273 simulating the interannual NAD pattern.

274 The relationship between the NAD and the AWP and the physical processes in
275 model simulations were subsequently analyzed. Figure 11 illustrates simulated lead-
276 lag correlations between DJFM-averaged NADI with 3-month-averaged AWP. A
277 conspicuous feature is that the lead-lag correlations of the 25 models show a chiefly
278 consistent trend. Qualitatively, most models (16 out of 25) replicate a significant
279 negative correlation occurring in spring or early summer. Concomitantly, more than
280 half of the models simulated a negative correlation passing the 90% significance level
281 between the previous winter NAD and following MJJ AWP as depicted in Figure 12.

282 Furthermore, Liu et al. (2013) highlighted that in observations, the maximum
283 effects of NAO and ENSO on AWP occur in boreal spring. Some models, such as
284 ACCESS-ESM1-5, BCC-CSM2-MR, MPI-ESM1-2-HR, and MPI-ESM1-2-LR,
285 faultily continue till summer, as shown in Figure 12. It is also affirmed that a marked
286 cold SST bias in the AWP region still exists in most CMIP3 and CMIP5 models, which
287 exhibit feeble AWP variability as represented by the AWP (Kozar and Misra 2013;
288 Liu et al. 2012). This might be the reason for the contradiction between the results
289 emanating from models and the recorded observations.

290 The aforementioned results denote that a significant negative correlation between
291 boreal winter NAD and following spring or early summer AWP variability can be
292 replicated in most CMIP6. The multi-model ensemble means (MME) of these models
293 will subsequently be employed to analyze the 3-month averaged SST and surface wind
294 anomalies with the NADI. As illustrated in Figure 13, a tripole-like SST pattern in the
295 North Atlantic and southwesterly abnormalities in TNA are discerned during the DJF.

296 These SST anomalies persist and reach maximum intensity in the MAM due to the WES
297 feedback. It is further noted that NAD-related TNA cooling is also widespread during
298 MJJ, extending from the Caribbean Sea to the Gulf of Mexico, with significant negative
299 values persisting to the JAS. However, the center of negative SST anomalies in TNA
300 from models is found to be more eastern than those from recorded observations, and
301 the southwesterly anomalies are significantly weakened after the MAM.

302 3.4 Climate effects

303 Numerous studies have yielded evidence of the importance of AWP in modulating
304 the climate system (Donders et al. 2011). For instance, the AWP acts as a source of
305 moisture for precipitation in Central and North America. During the development and
306 the persistence of the large summer AWP, the North Atlantic brings about increasing
307 temperatures recorded in Florida (Drumond et al. 2011; Liu et al. 2015). Factoring in
308 the relationship between the NAD and the AWP, the winter NAD may influence the
309 North Atlantic region's climate effects through its impact on the AWP in the following
310 months.

311 The correlation of DJFM-averaged NADI with precipitation, 700hPa relative
312 humidity, and surface air temperature anomalies in the following summer (the JJA
313 season) has been calculated to try this hypothesis. As depicted in Figure 14a, the region
314 with markedly lower precipitation frequencies associated with previous winter NAD
315 covers the southern Gulf of Mexico, Caribbean Sea, and TNA during summer, recent
316 corroborating research (Zhou et al. 2019). Meanwhile, the relative humidity field at

317 700hPa exhibits zonal distribution characteristics (Fig. 14b). Consequential positive
318 correlations are found in southwest North America, the Gulf of Mexico, and the
319 southeastern Pacific Ocean. Meanwhile, significant negative correlations are in the area
320 around between the north of the equator and south of 20°N. The region with high
321 temperature is linked to low precipitation frequencies, exceptionally better in TNA (Fig.
322 14c).

323 Conversely, the area with significantly lower precipitation frequencies associated
324 with previous winter NAD by linearly removing the following MJJ AWPI is noticeably
325 smaller, restrained to the Gulf of Mexico (Fig. 14d). The relative humidity field
326 delineates the weakening effect of NAD on summer precipitation in the TNA region
327 (Fig. 14e). The air temperature in the Caribbean Sea and western TNA region are
328 significantly affected following the removal of the signal. As per the aforementioned
329 analysis, the winter NAD-like atmospheric signal may be stored in the following AWP,
330 thus notably influencing the TNA precipitation and air temperature in summer. The
331 AWP may act as a bridge connecting winter NAD to the subsequent summer
332 precipitation and air temperature in the TNA region.

333 3.5 Prediction model

334 Given that the winter NAD has a major influence on the summer precipitation over
335 western TNA (85°W–50°W, 10°–25°N) through its impact on the following AWP, the
336 winter NAD and the following MJJ AWP can be exploited to foretell summer
337 precipitation over this region. Therefore, a simple empirical prediction model was

338 established to predict the summer [JJA (+1)] precipitation (referred to as precipitation
339 index, PI) over western TNA by using the DJFM (0) NADI and the MJJ (+1) AWPAL.
340 The model is based on a linear regression method, choosing the DJFM (0) NADI and
341 MJJ (+1) AWPAL as variables. The formula is as follows:

$$342 \quad PI(t + 1) = \alpha \times NADI(t) + \beta \times AWPAL(t), \quad (2)$$

343 where the parameters α and β are calculated by a least-squares fit to the DJFM (0)
344 NADI and MJJ (+1) AWPAL, respectively. The time series of $PI(t + 1)$, $NADI(t)$,
345 and $AWPAL(t)$ have been standardized.

346 To evaluate the prediction virtues of this model, the fourfold cross-validation was
347 conducted. As illustrated in Figure 15b, the correlations between the observed values
348 and fourfold cross-validated hindcasts were slightly lower than those shown in Figure
349 15a. However, they are still statistically significant in the critical areas of research. The
350 time series of observed JJA (+1) PI and cross-validated hindcasted JJA (+1) PI are
351 displayed in Figure 15c. The highly significant correlation ($R=0.72$) between the
352 observations and the cross-validated hindcasts indicates the relatively good reliability
353 of our model. Thus, it is practical to utilize this model to simulate the summer
354 precipitation over the western TNA region.

355 **4. Summary and Discussion**

356 The focus of this study was to assay the link between the North American dipole
357 (NAD) and AWP. The maximum effects of winter NAD on AWP were found to manifest
358 in late spring or early summer (MJJ), as proved by significant correlations of the

359 wintertime NAD index with the AWP indices (including the AWP_{AI} and AWP_{DI}). The
360 strong positive (negative) phase of the winter NAD tends to inhibit (favor) the
361 development of AWP in its area and depth in the subsequent months. In contrast with
362 the NAD, the previous winter NAO has little effect on the following size and depth of
363 AWP, inferring that AWP variability may be relatively more of a lagging response to
364 NAD atmospheric forcing rather than a lagging response to NAO atmospheric forcing.

365 A probable reason for this phenomenon is that the winter NAD can induce SST
366 cooling over the TNA region during spring due to WES feedback. Henceforth, the
367 primary factor appears to be the persistence of the TNA SST cooling. The NAD-related
368 TNA cooling is also extensive during MJJ, expanding from the Caribbean to the Gulf
369 of Mexico with significant negative values lasting well into the following year's
370 summer months. It is also affirmed by modeling coupled model experiments to confirm
371 further that the winter NAD influences the subsequent AWP development.

372 Most CMIP6 models were found to underestimate the NAD pattern. A significant
373 negative correlation between boreal winter NAD and next spring or early summer AWP
374 variability can be reproduced in most CMIP6 models. Furthermore, the MME of
375 CMIP6 models confirms that the NAD-related TNA cooling lasts from the spring into
376 the summer months of the following year.

377 Moreover, the winter NAD-like atmospheric signal may be stored in the following
378 AWP, thus having a commanding influence on the TNA precipitation and air
379 temperature in summer. It is hypothesized that the AWP may act as a bridge linking
380 winter NAD to the following summer precipitation and air temperature in the TNA

381 region. It is deduced that DJFM NAD and MJJ AWP can be an effective forecaster of
382 following summer precipitation over western TNA. However, assiduous research is
383 required to assign more predictors of summer precipitation over TNA.

384

385

386 *Acknowledgments*

387 This work was jointly supported by the National Natural Science Foundation of
388 China (grant number 41975070 and 41790474).

389

References

390

391 Behringer, D. W., Ji, M., and Leetmaa, A. (1998). An improved coupled model for
392 ENSO prediction and implications for ocean initialization. Part I: The ocean data
393 assimilation system. *Monthly Weather Review*, 126(4), 1013-1021.

394 Bretherton, C. S., Widmann, M., Dymnikov, V. P., Wallace, J. M., and Bladé, I. (1999).
395 The effective number of spatial degrees of freedom of a time-varying field.
396 *Journal of Climate*, 12(7), 1990-2009.

397 Covey, D. L., and Hastenrath, S. (1978). The Pacific El Nino phenomenon and the
398 Atlantic circulation. *Monthly Weather Review*, 106(9), 1280-1287.

399 Curtis, S., and Hastenrath, S. (1995). Forcing of anomalous sea surface temperature
400 evolution in the tropical Atlantic during Pacific warm events. *Journal of*
401 *Geophysical Research: Oceans*, 100(C8), 15835-15847.

402 Czaja, A., Van der Vaart, P., and Marshall, J. (2002). A diagnostic study of the role of
403 remote forcing in tropical Atlantic variability. *Journal of Climate*, 15(22), 3280-
404 3290.

405 Curtis, S. (2013). Daily precipitation distributions over the intra-Americas sea and their
406 interannual variability. *Atmósfera*, 26(2), 243-259.

407 Durán-Quesada, A. M., Gimeno, L., Amador, J., and Nieto, R. (2010). Moisture sources
408 for Central America: Identification of moisture sources using a Lagrangian
409 analysis technique. *Journal of Geophysical Research: Atmospheres*, 115(D5).

410 Donders, T. H., de Boer, H. J., Finsinger, W., Grimm, E. C., Dekker, S. C., Reichart, G.
411 J., et al. (2011). Impact of the Atlantic Warm Pool on precipitation and temperature
412 in Florida during North Atlantic cold spells. *Climate Dynamics*, 36(1-2), 109-118.

413 Drumond, A., Nieto, R., and Gimeno, L. (2011). On the contribution of the Tropical
414 Western Hemisphere Warm Pool source of moisture to the Northern Hemisphere
415 precipitation through a Lagrangian approach. *Journal of Geophysical Research:*
416 *Atmospheres*, 116(D21).

417 Ding, R., Li, J., Tseng, Y. H., Sun, C., and Zheng F. (2017). Linking a sea level pressure
418 anomaly dipole over North America to the central Pacific El Niño. *Climate*
419 *Dynamics*, 49(4), 1321-1339.

420 Ding, R., Li, J., Tseng, Y. H., Sun, C., Li, Y., Xing, N., et al. (2019). Linking the North
421 American dipole to the Pacific meridional mode. *Journal of Geophysical Research:*
422 *Atmospheres*, 124(6), 3020-3034.

423 Enfield, D. B. (1996). Relationships of inter-American rainfall to tropical Atlantic and
424 Pacific SST variability. *Geophysical Research Letters*, 23(23), 3305-3308.

425 Enfield, D. B., and Mayer, D. A. (1997). Tropical Atlantic sea surface temperature
426 variability and its relation to El Niño-Southern Oscillation. *Journal of Geophysical*
427 *Research: Oceans*, 102(C1), 929-945.

428 Enfield, D. B., Lee, S. K., and Wang, C. (2006). How are large western hemisphere
429 warm pools formed? *Progress in Oceanography*, 70(2-4), 346-365.

430 Eyring, V., Bony, S., Meehl, G. A., Senior, C. A., Stevens, B., Stouffer, R. J., et al.
431 (2016). Overview of the Coupled Model Intercomparison Project Phase 6 (CMIP6)

432 experimental design and organization. *Geoscientific Model Development*, 9(5),
433 1937-1958.

434 Giannini, A., Kushnir, Y., and Cane, M. A. (2000). Interannual variability of Caribbean
435 rainfall, ENSO, and the Atlantic Ocean. *Journal of Climate*, 13(2), 297-311.

436 Giannini, A., Cane, M. A., and Kushnir, Y. (2001). Interdecadal changes in the ENSO
437 teleconnection to the Caribbean region and the North Atlantic Oscillation. *Journal*
438 *of Climate*, 14(13), 2867-2879.

439 Kalnay, E., Kanamitsu, M., Kistler, R., Collins, W., Deaven, D., Gandin, L., et al. (1996).
440 The NCEP/NCAR 40-year reanalysis project. *Bulletin of the American*
441 *Meteorological Society*, 77(3), 437-472.

442 Kozar, M. E., and Misra, V. (2013). Evaluation of twentieth-century Atlantic Warm Pool
443 simulations in historical CMIP5 runs. *Climate Dynamics*, 41(9-10), 2375-2391.

444 Li, J., and Wang, J. X. (2003). A new North Atlantic Oscillation index and its variability.
445 *Advances in Atmospheric Sciences*, 20(5), 661-676.

446 Li, L., Lin, P., Yu, Y., Wang, B., Zhou, T., Liu, L., et al. (2003). The flexible global
447 ocean-atmosphere-land system model, grid-point version 2: FGOALS-g2.
448 *Advances in Atmospheric Sciences*, 30(3), 543-560.

449 Liu, H., Wang, C., Lee, S. K., and Enfield, D. (2012). Atlantic warm pool variability in
450 the IPCC AR4 CGCM simulations. *Journal of Climate*, 25(16), 5612-5628.

451 Liu, H., Wang, C., Lee, S. K., and Enfield, D. (2013). Atlantic warm pool variability in
452 the CMIP5 simulations. *Journal of Climate*, 26(15), 5315-5336.

453 Liu, H., Wang, C., Lee, S. K., and Enfield, D. (2015). Inhomogeneous influence of the
454 Atlantic warm pool on United States precipitation. *Atmospheric Science Letters*,
455 16(1), 63-69.

456 Mo, K. C., and Häkkinen, S. (2001). Interannual variability in the tropical Atlantic and
457 linkages to the Pacific. *Journal of Climate*, 14(12), 2740-2762.

458 Misra, V., Stroman, A., and DiNapoli, S. (2013). The rendition of the Atlantic Warm
459 Pool in the reanalyses. *Climate Dynamics*, 41(2), 517-532.

460 Misra, V., Groenen, D., Bhardwaj, A., and Mishra, A. (2016). The warm pool variability
461 of the tropical northeast Pacific. *International Journal of Climatology*, 36(14),
462 4625-4637.

463 Nobre, P., and Shukla, J. (1996). Variations of sea surface temperature, wind stress, and
464 rainfall over the tropical Atlantic and South America. *Journal of Climate*, 9(10),
465 2464-2479.

466 Rayner, N., Parker, D. E., Horton, E., Folland, C. K., Alexander, L. V., Rowell, D., et
467 al. (2003). Global analyses of sea surface temperature, sea ice, and night marine
468 air temperature since the late nineteenth century. *Journal of Geophysical Research:*
469 *Atmospheres*, 108(D14).

470 Taylor, K. E. (2001). Summarizing multiple aspects of model performance in a single
471 diagram. *Journal of Geophysical Research: Atmospheres*, 106(D7), 7183-7192.

472 Webster, P. J., and Lukas, R. (1992). TOGA COARE: The coupled ocean-atmosphere
473 response experiment. *Bulletin of the American Meteorological Society*, 73(9),
474 1377-1416.

475 Wang, C., and Enfield, D. B. (2001). The tropical Western Hemisphere warm pool.
476 *Geophysical Research Letters*, 28(8), 1635-1638.

477 Wang, C., and Enfield, D. B. (2003). A further study of the tropical Western Hemisphere
478 warm pool. *Journal of Climate*, 16(10), 1476-1493.

479 Wang, C., Enfield, D. B., Lee, S.-K., and Landsea, C. W. (2006). Influences of the
480 Atlantic warm pool on Western Hemisphere summer rainfall and Atlantic
481 hurricanes. *Journal of Climate*, 19(12), 3011-3028.

482 Wang, C., and Lee, S.-K. (2007). Atlantic warm pool, Caribbean low-level jet, and their
483 potential impact on Atlantic hurricanes. *Geophysical Research Letters*, 34(2).

484 Wang, C., and Lee, S.-K. (2008). Global warming and United States landfalling
485 hurricanes. *Geophysical Research Letters*, 35(2).

486 Wang, C., Lee, S.-K., and Enfield, D. B. (2008a). Atlantic warm pool acting as a link
487 between Atlantic multidecadal oscillation and Atlantic tropical cyclone activity.
488 *Geochemistry, Geophysics, Geosystems*, 9(5).

489 Wang, C., Lee, S.-K., and Enfield, D. B. (2008b). Climate response to anomalously
490 large and small Atlantic warm pools during the summer. *Journal of Climate*,
491 21(11), 2437-2450.

492 Wang, C., Liu, H., Lee, S.-K., and Atlas, R. (2011). Impact of the Atlantic warm pool
493 on United States landfalling hurricanes. *Geophysical Research Letters*, 38(19).

494 Xie, S.-P., and Philander, S. G. H. (1994). A coupled ocean-atmosphere model of
495 relevance to the ITCZ in the eastern Pacific. *Tellus A*, 46(4), 340-350.

496 Xie, P., and Arkin, P. A. (1997). Global precipitation: A 17-year monthly analysis based
497 on gauge observations, satellite estimates, and numerical model outputs. *Bulletin*
498 *of the American Meteorological Society*, 78(11), 2539-2558.

499 Zhou, X., Wang, W., Ding, R., Li, J., Hou, Z., and Xie, W. (2019). An Investigation of
500 the Differences between the North American Dipole and North Atlantic Oscillation.

501 *Atmosphere*, 10(2), 58.

502

503 **Figure Captions**

504

505 **Figure 1.** (a) Maps of correlation between the DJFM-averaged SLP anomalies and the
506 simultaneous NADI (blue lines) and NAOI (red lines). The contour interval is
507 0.1. Only correlations greater than 0.5 are shown; (b) the interannual time series
508 of the DJFM-averaged NADI (blue line) and NAOI (red line). The horizontal
509 dashed lines indicate ± 1 standard deviation. The correlation coefficient (R)
510 between the NADI and NAOI is shown in the top left corner.

511 **Figure 2.** Correlation maps of the DJFM-averaged air temperature (shading, units: $^{\circ}\text{C}$)
512 and wind (vectors, units: ms^{-1}) anomalies with the simultaneous NADI at 1000hPa,
513 925hPa and 850hPa. Positive (red) and negative (blue) air temperature anomalies
514 with correlations significant at or above the 90% confidence level are shaded. Only
515 wind vectors significant at the 90% confidence level are shown.

516 **Figure 3.** (a) Lead-lag correlations of the DJFM (0)-averaged NAD index (red line) and
517 NAO index (yellow line) with 3-month-averaged AWP area index (red line). (b)
518 As in (a), but with 3-month-averaged AWP depth index. The horizontal dashed
519 line shows the 99% confidence level.

520 **Figure 4.** (a) Spatial pattern of DJFM-averaged sea level pressure anomalies correlated
521 with the following MJJ AWPDI. (b) As in (a), but with the following MJJ AWPDI.
522 Positive (yellow) and negative (blue) SLP anomalies with correlations significant
523 at or above the 95 % confidence level are shaded and the contour interval is 0.1.

524 **Figure 5.** (a)-(c) Seasonal 3-month-averaged distributions of SST of the 28.5°C

525 isotherm; (d)-(f) composite of following 3-month-averaged SST of the 28.5°C
526 isotherm from positive NAD cases (red line) and negative NAD cases (blue line);
527 (h)-(j) as in (d)-(f) but from positive NAO cases (red line) and negative NAO cases
528 (blue line).

529 **Figure 6.** (a)-(c) Composite of following 3-month-averaged depth (m) of the 28.5°C
530 isotherm from positive NAD cases; (d)-(f) as in (a)-(c) but from negative NAD
531 cases.

532 **Figure 7.** Correlation maps of the DJFM-averaged NADI with the 3-month averages
533 of SST (shading, units: °C), surface wind (vectors, units: m\s) anomalies for (a)
534 DJF, (b) MAM, (c) MJJ and (d) JAS. Positive (red) and negative (blue) SST
535 anomalies with correlations significant at or above the 90% confidence level are
536 stippled. Only surface wind vectors significant at the 90% confidence level are
537 shown. The green box area indicates the extent of the AWP.

538 **Figure 8.** Composite differences in the seasonal evolution of SST (shading, units: °C)
539 and surface wind (vectors, units: m\s) anomalies between the assimilation and
540 control experiments for (a) DJF, (b) MAM, (c) MJJ and (d) JAS. Positive (red) and
541 negative (blue) SST anomalies with correlations significant at or above the 90%
542 confidence level are stippled. Only surface wind vectors significant at the 90%
543 confidence level are shown. The green box area indicates the extent of the AWP.

544 **Figure 9.** Spatial pattern of DJFM-averaged SLP anomalies correlated with the
545 concurrent NADI derived from observation and the 25 CMIP6 model simulations.

546 **Figure 10.** Taylor diagram of the NAD pattern. Each numbered dot in the diagram
547 represents a single model. The term “REF” on the horizontal axis refers to the
548 reference point. Black dashed lines and arcs indicate the correlation coefficient
549 and the ratio of standard deviations between modeled and observed NAD patterns,
550 respectively. Black solid arcs show the centered root mean square difference which
551 is equal to the radical distance from the reference point.

552 **Figure 11.** Lead-lag correlations of the DJFM (0)-averaged NADI with 3-month-
553 averaged AWPPI derived from the CMIP6 model simulations. The horizontal
554 dashed lines show the 90% confidence levels.

555 **Figure 12.** Correlations of the DJFM (0)-averaged NADI with following MJJ AWPPI
556 derived from the CMIP6 model simulations. The horizontal dashed lines show the
557 90% confidence levels.

558 **Figure 13.** As in Figure 8 but for correlation maps of the 3-month averaged SST
559 (shading) and surface wind (vectors) anomalies with the NADI derived from the
560 MME of CMIP6 model simulations.

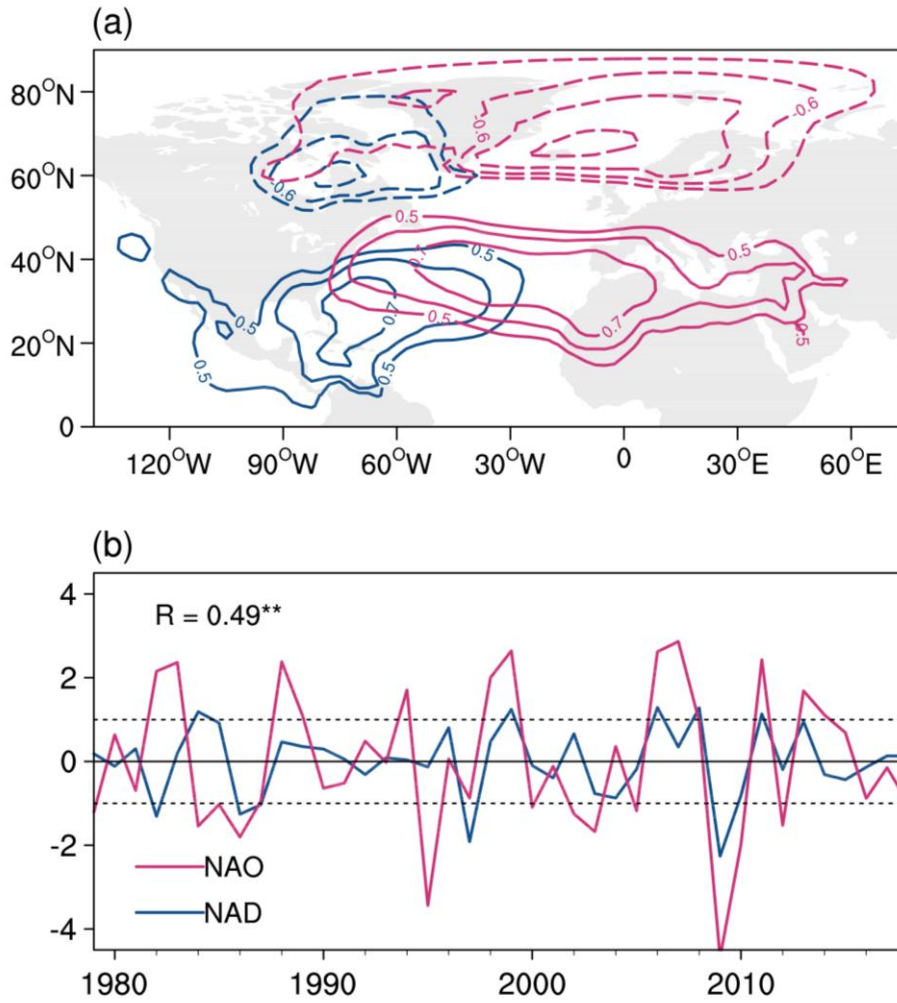
561 **Figure 14.** (a)-(c) Correlation map of the summer (the JJA season) precipitation (units:
562 mm/d) anomalies, 700hPa relative humidity anomalies and surface air temperature
563 (units: °C) anomalies with the DJFM-averaged NADI. (d)-(f) as in (a)-(c) but for
564 the DJFM-averaged NADI linearly removing the following MJJ AWPPI.

565 **Figure 15.** (a) Correlation between the observed and hindcast JJA (+1) precipitation
566 anomalies obtained from the empirical prediction model. (b) Correlation between
567 observations and fourfold cross-validated hindcasts of JJA (+1) precipitation

568 anomalies. Only areas with correlations significant at the 90% level are shown. (c)

569 Time series of observed and fourfold cross-validated hindcast JJA (+1) PI.

570

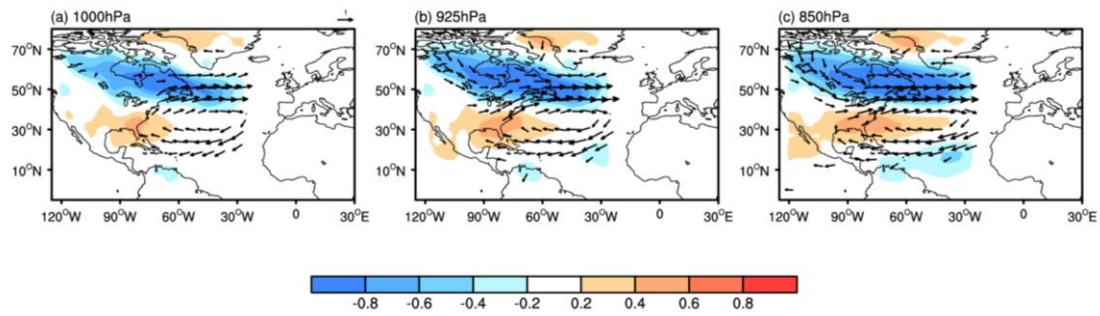


571

572 **Figure 1.** (a) Maps of correlation between the DJFM-averaged SLP anomalies and the
 573 simultaneous NADI (blue lines) and NAOI (red lines). The contour interval is 0.1. Only
 574 correlations greater than 0.5 are shown. (b) the interannual time series of the DJFM-
 575 averaged NADI (blue line) and NAOI (red line). The horizontal dashed lines indicate
 576 ± 1 standard deviation. The correlation coefficient (R) between the NADI and NAOI is
 577 shown in the top left corner.

578

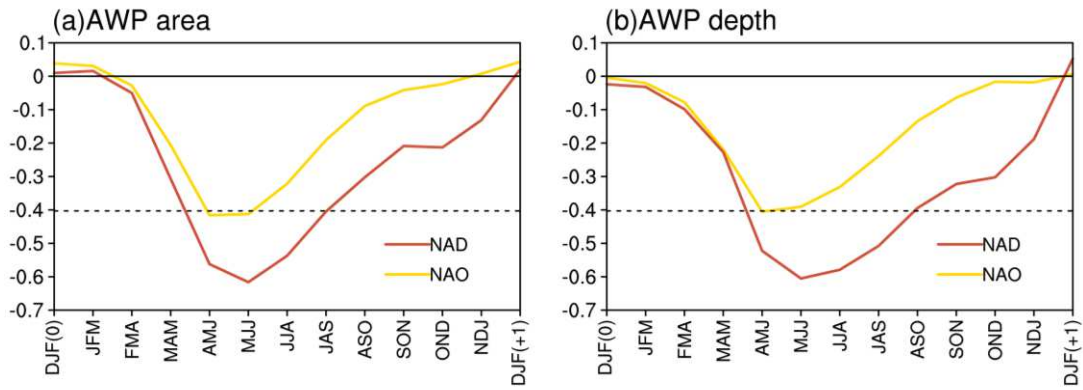
579



580

581 **Figure 2.** Correlation maps of the DJFM-averaged air temperature (shading, units: °C)
 582 and wind (vectors, units: m/s) anomalies with the simultaneous NADI at 1000hPa,
 583 925hPa and 850hPa. Positive (red) and negative (blue) air temperature anomalies with
 584 correlations significant at or above the 90% confidence level are shaded. Only wind
 585 vectors significant at the 90% confidence level are shown.

586

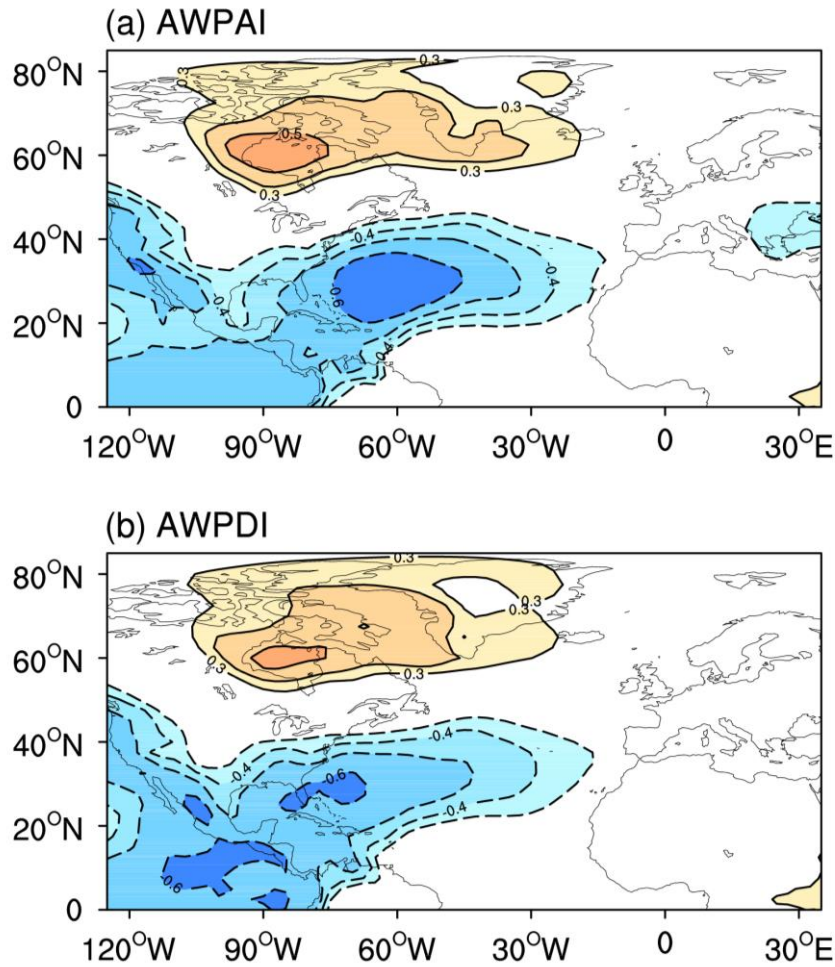


587

588 **Figure 3.** (a) Lead-lag correlations of the DJFM (0)-averaged NAD index (red line) and
 589 NAO index (yellow line) with 3-month-averaged AWP area index (red line). (b) As in
 590 (a), but with 3-month-averaged AWP depth index. The horizontal dashed line shows the
 591 99% confidence level.

592

593



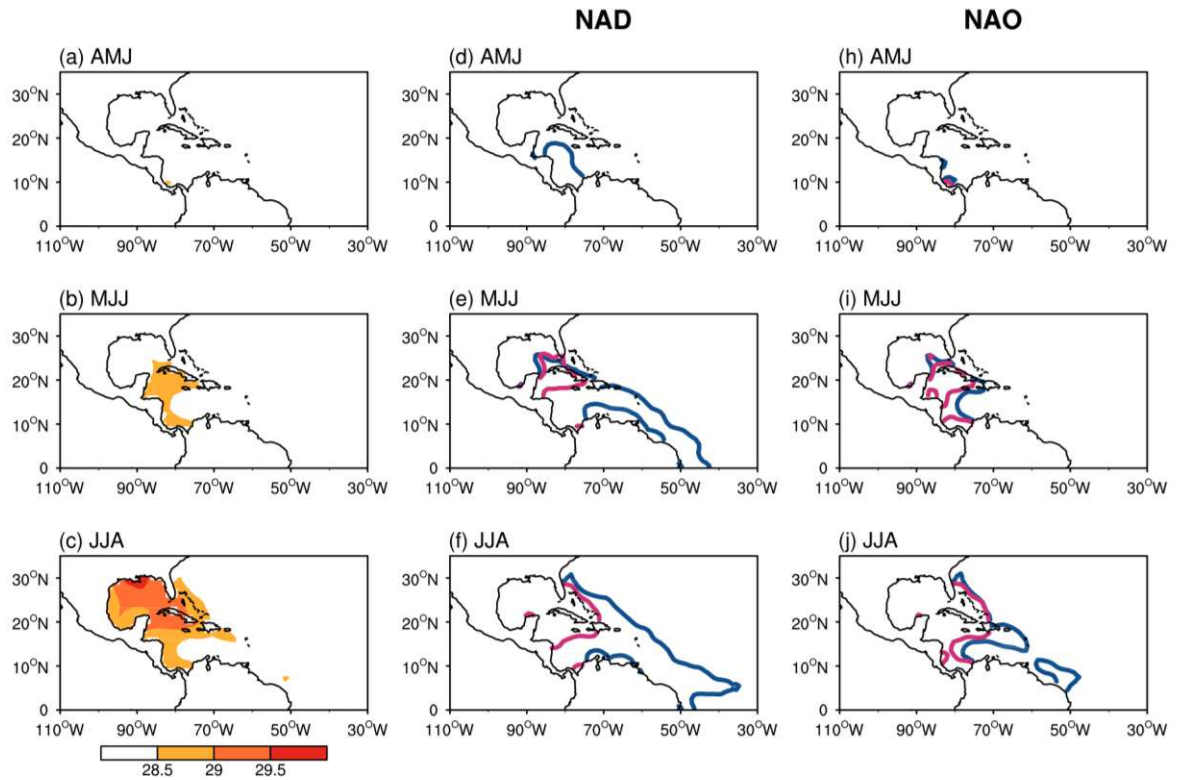
594

595 **Figure 4.** (a) Spatial pattern of DJFM-averaged sea level pressure anomalies correlated

596 with the following MJJ AWPPI. (b) As in (a), but with the following MJJ AWPDI.

597 Positive (yellow) and negative (blue) SLP anomalies with correlations significant at or

598 above the 95 % confidence level are shaded and the contour interval is 0.1.



599

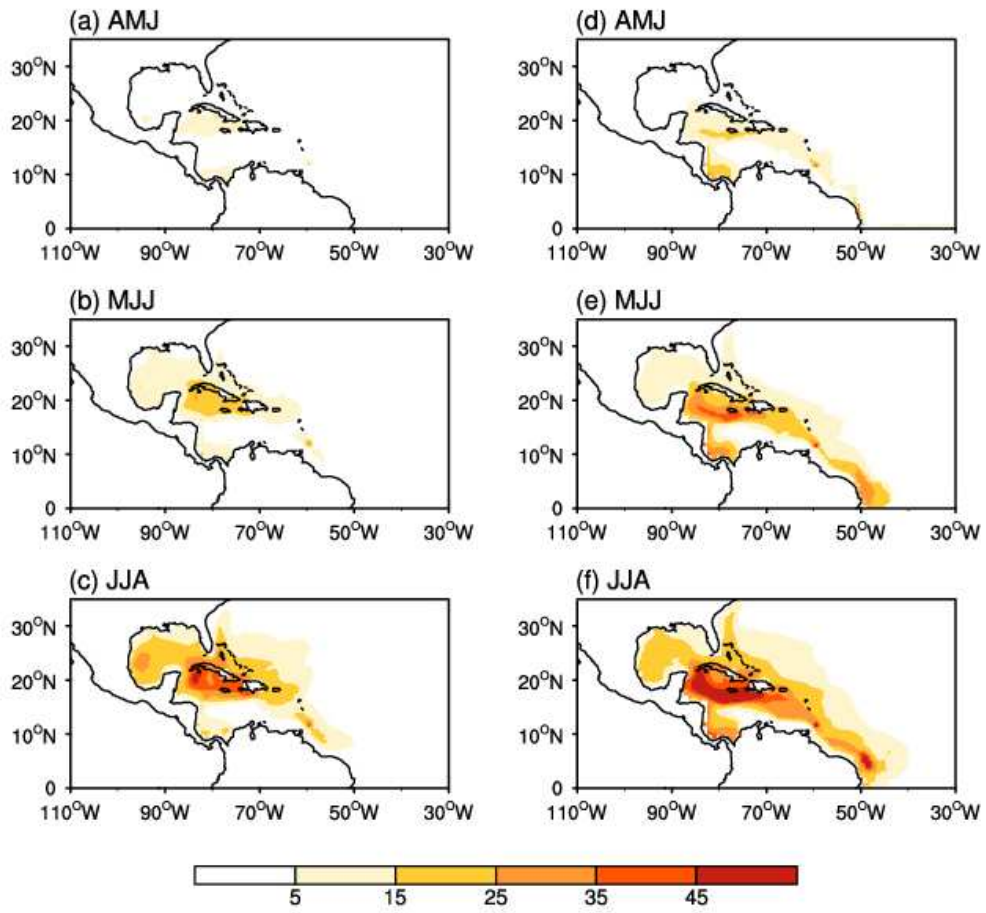
600 **Figure 5.** (a)-(c) Seasonal 3-month-averaged distributions of SST of the 28.5°C

601 isotherm; (d)-(f) composite of following 3-month-averaged SST of the 28.5°C isotherm

602 from positive NAD cases (red line) and negative NAD cases (blue line); (h)-(j) as in

603 (d)-(f) but from positive NAO cases (red line) and negative NAO cases (blue line).

604

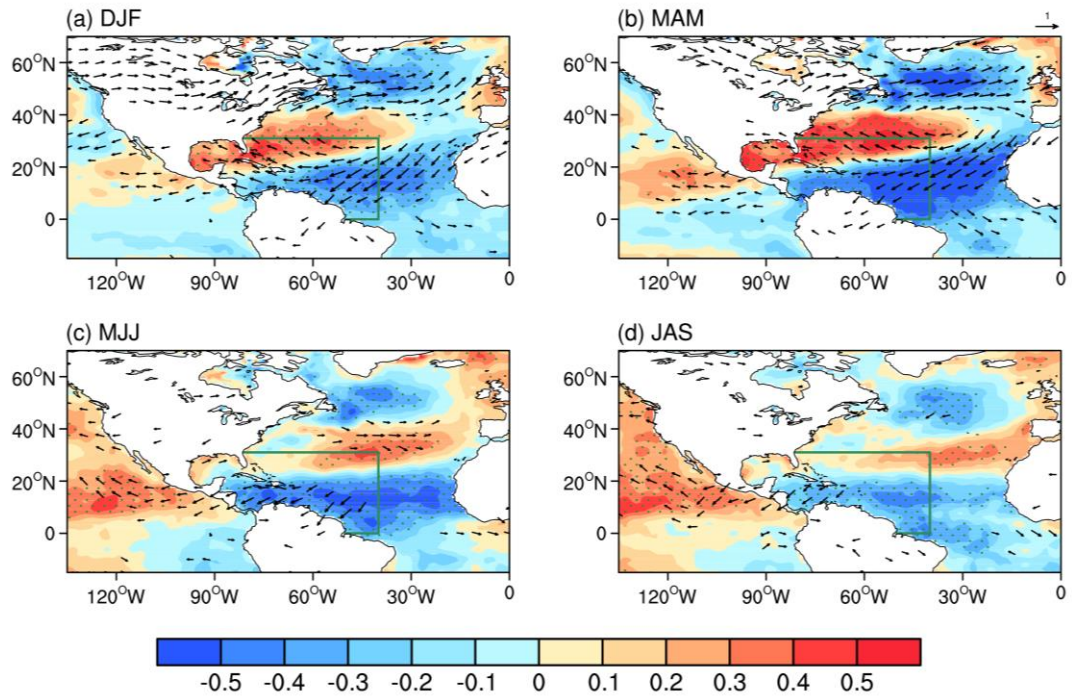


605

606 **Figure 6.** (a)-(c) Composite of following 3-month-averaged depth (m) of the 28.5°C

607 isotherm from positive NAD cases; (d)-(f) as in (a)-(c) but from negative NAD cases.

608

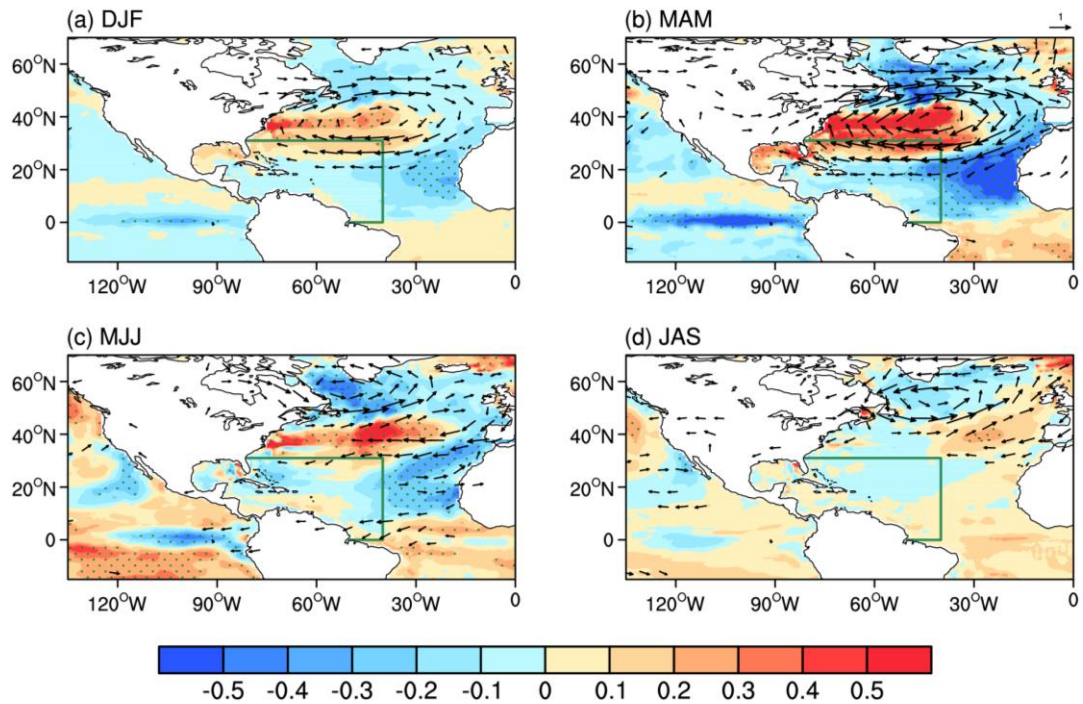


609

610 **Figure 7.** Correlation maps of the DJFM-averaged NADI with the 3-month averages
 611 of SST (shading, units: °C), surface wind (vectors, units: m/s) anomalies for (a) DJF,
 612 (b) MAM, (c) MJJ and (d) JAS. Positive (red) and negative (blue) SST anomalies with
 613 correlations significant at or above the 90% confidence level are stippled. Only surface
 614 wind vectors significant at the 90% confidence level are shown. The green box area
 615 indicates the extent of the AWP.

616

617



618

619 **Figure 8.** Composite differences in the seasonal evolution of SST (shading, units: °C)

620 and surface wind (vectors, units: m/s) anomalies between the assimilation and control

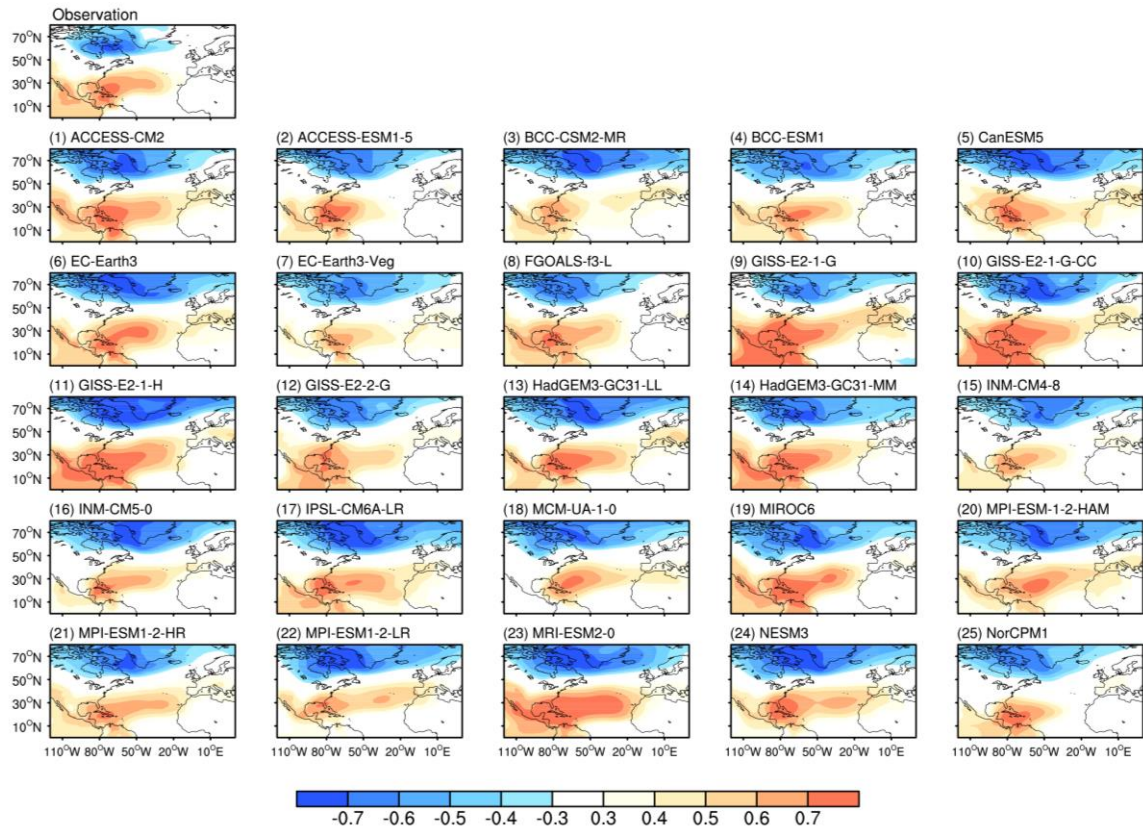
621 experiments for (a) DJF, (b) MAM, (c) MJJ and (d) JAS. Positive (red) and negative

622 (blue) SST anomalies with correlations significant at or above the 90% confidence level

623 are stippled. Only surface wind vectors significant at the 90% confidence level are

624 shown. The green box area indicates the extent of the AWP.

625

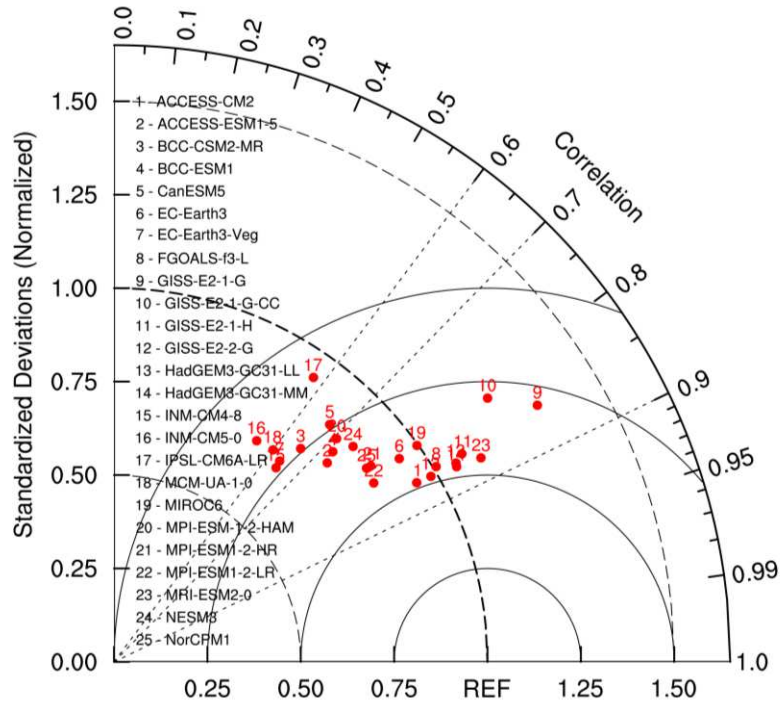


626

627 **Figure 9.** Spatial pattern of DJFM-averaged SLP anomalies correlated with the

628 concurrent NADI derived from observation and the 25 CMIP6 model simulations.

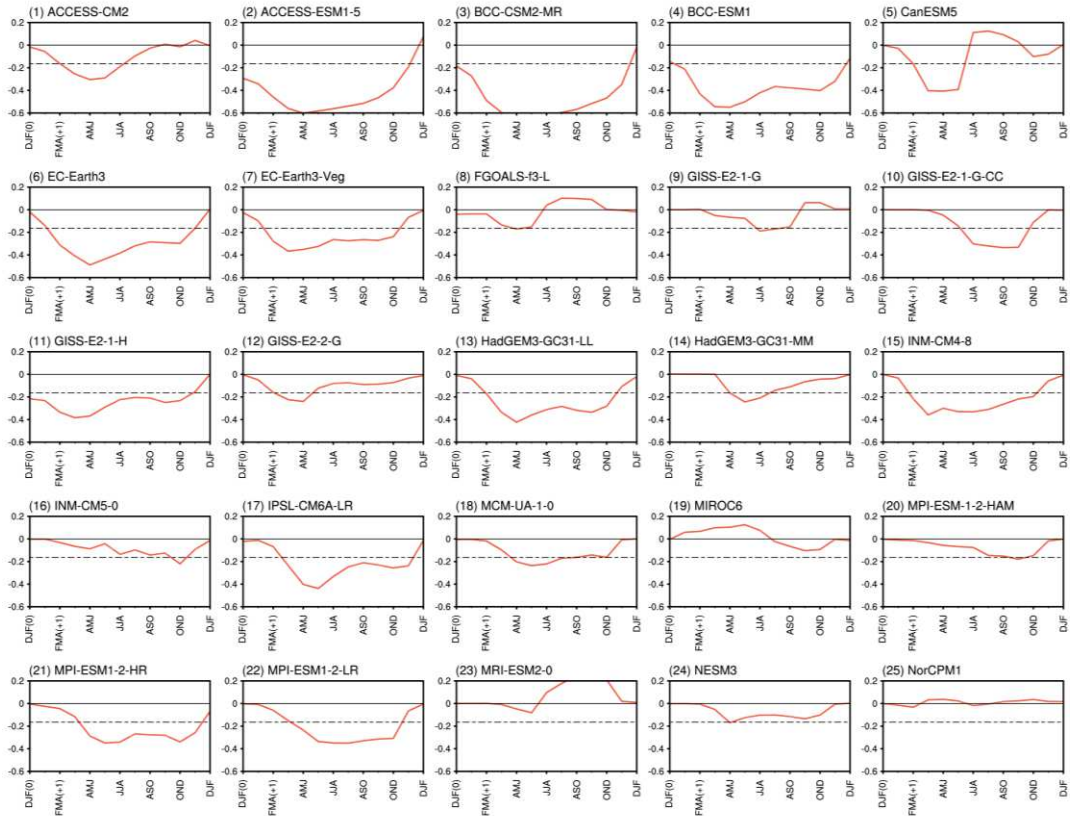
629



630

631 **Figure 10.** Taylor diagram of the NAD pattern. Each numbered dot in the diagram
 632 represents a single model. The term “REF” on the horizontal axis refers to the reference
 633 point. Black dashed lines and arcs indicate the correlation coefficient and the ratio of
 634 standard deviations between modeled and observed NAD patterns, respectively. Black
 635 solid arcs show the centered root mean square difference which is equal to the radical
 636 distance from the reference point.

637



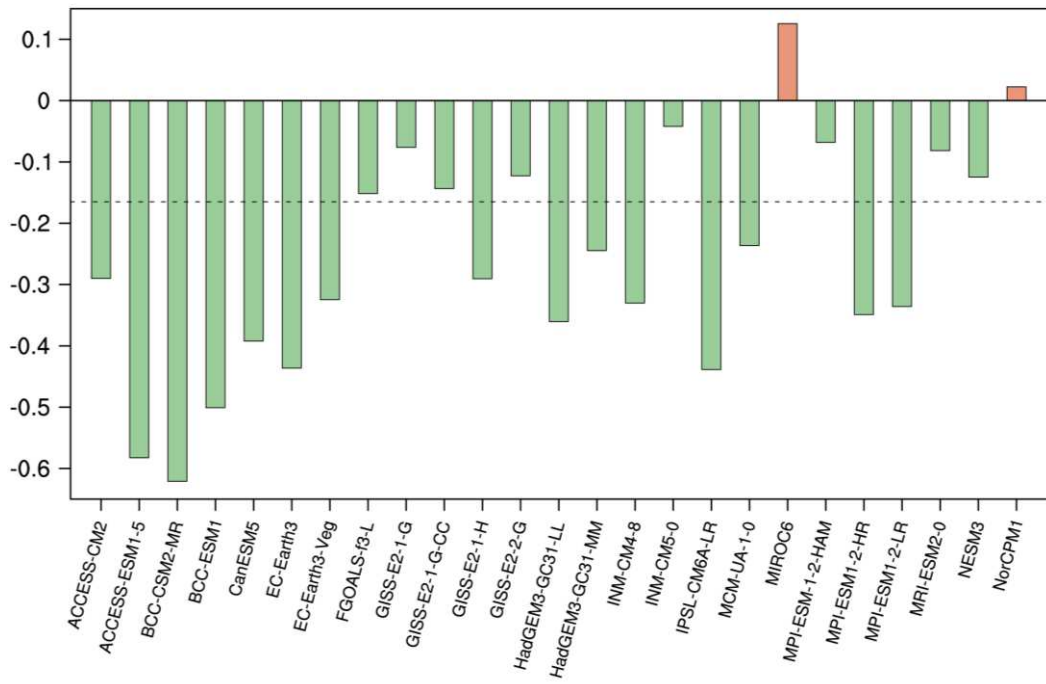
638

639 **Figure 11.** Lead-lag correlations of the DJFM (0)-averaged NADI with 3-month-

640 averaged AWPAl derived from the CMIP6 model simulations. The horizontal dashed

641 lines show the 90% confidence levels.

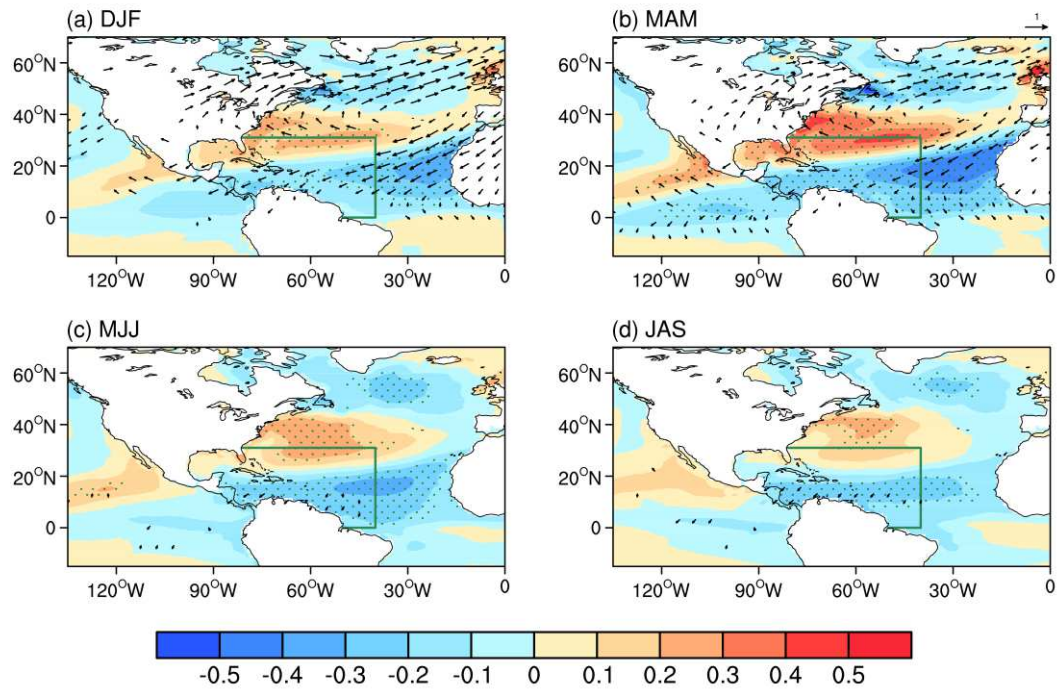
642



643

644 **Figure 12.** Correlations of the DJFM (0)-averaged NADI with following MJJ AWPI
 645 derived from the CMIP6 model simulations. The horizontal dashed lines show the 90%
 646 confidence levels.

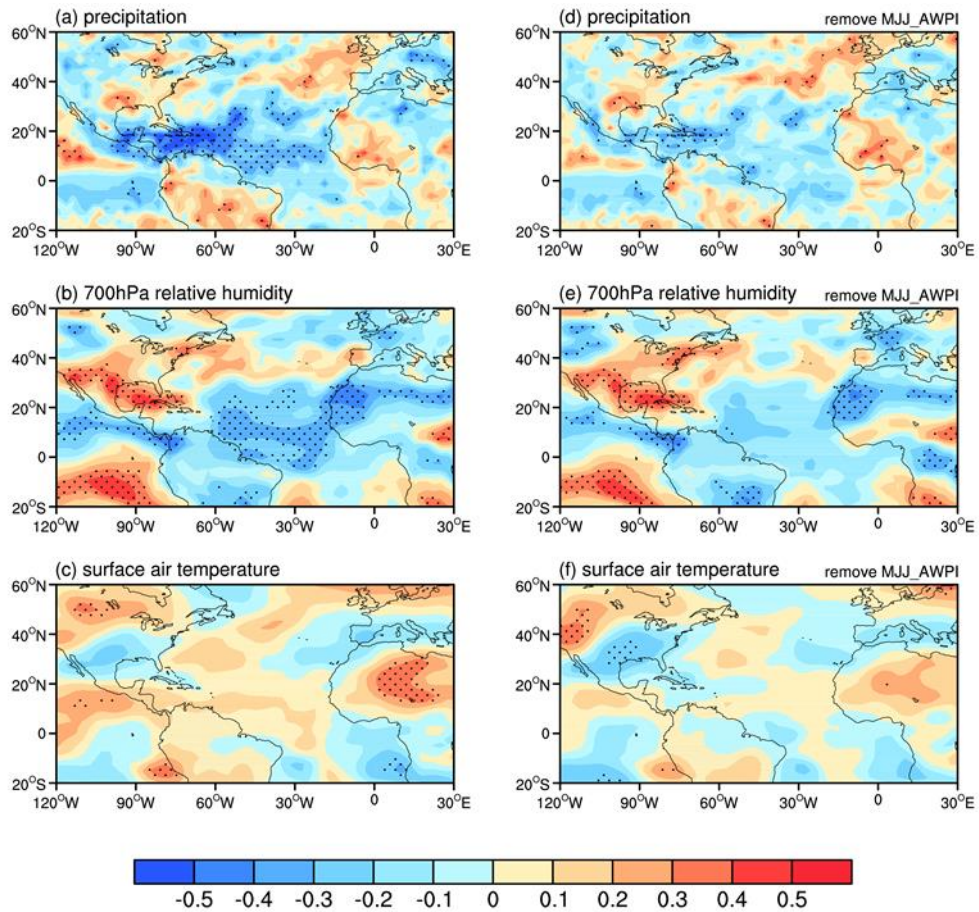
647



648

649 **Figure 13.** As in Figure 8 but for correlation maps of the 3-month averaged SST
 650 (shading) and surface wind (vectors) anomalies with the NADI derived from the MME
 651 of CMIP6 model simulations.

652



653

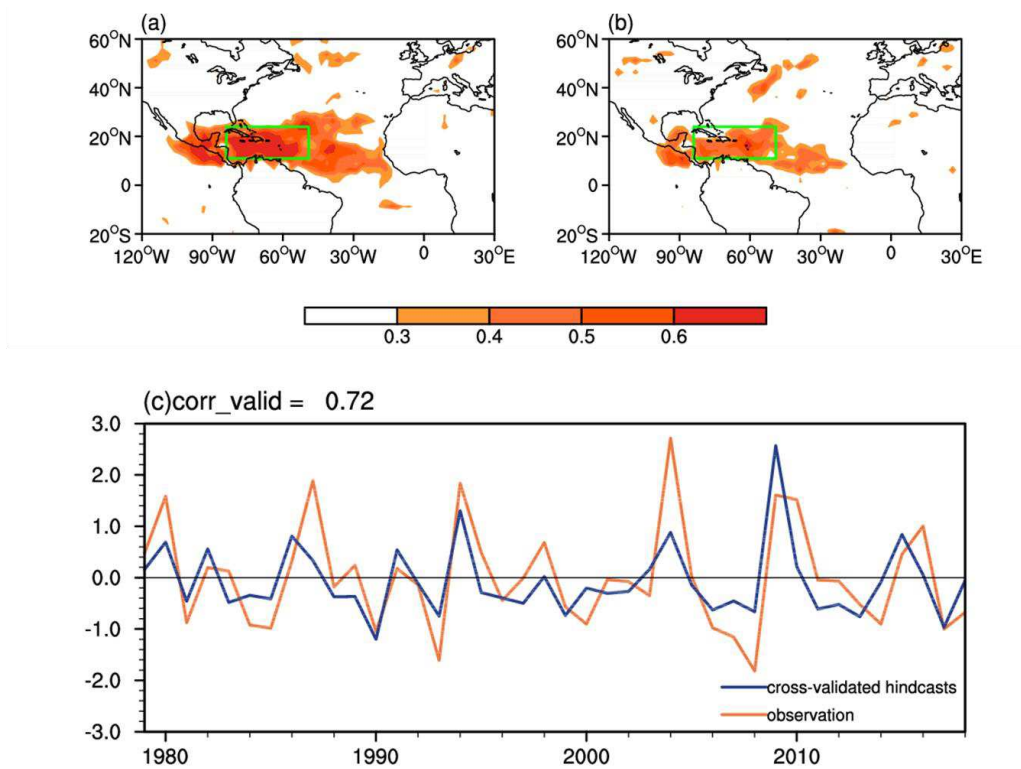
654 **Figure 14.** (a)-(c) Correlation map of the summer (the JJA season) precipitation (units:

655 mm/d) anomalies, 700hPa relative humidity anomalies and surface air temperature

656 (units: °C) anomalies with the DJFM-averaged NADI. (d)-(f) as in (a)-(c) but for the

657 DJFM-averaged NADI linearly removing the following MJJ AWPI.

658



659

660 **Figure 15.** (a) Correlation between the observed and hindcast JJA (+1) precipitation
 661 anomalies obtained from the empirical prediction model. (b) Correlation between
 662 observations and fourfold cross-validated hindcasts of JJA (+1) precipitation anomalies.
 663 Only areas with correlations significant at the 90% level are shown. (c) Time series of
 664 observed and fourfold cross-validated hindcast JJA (+1) PI.

665

666

667

668 **Table 1.** Classification of years in which positive (negative) NAD events

	positive NAD	negative NAD
years	1988, 1989, 1990, 1991, 2002, 2006	1982, 1983, 1995, 1997, 2009, 2010

669

Table 2. Description of CMIP6 models used in the study

Number	Model name	Model center	Resolution (lon×lat)	
			Atmosphere	Ocean
1	ACCESS-CM2	CSIRO-ARCCSS/Australia	1.88°×1.25°	1.00°×1.00°
2	ACCESS-ESM1-5	CSIRO/Australia	1.88°×1.25°	1.00°×1.00°
3	BCC-CSM2-MR	BCC/China	1.00°×0.74°	1.00° × (0.33°-1.00°)
4	BCC-ESM1	BCC/China	1.00°×0.74°	1.00° × (0.33°-1.00°)
5	CanESM5	CCCma/Canada	2.81°×2.79°	1.00° × (0.33°-1.00°)
6	EC-Earth3	EC-Earth-Consortium/EU	0.70°×0.70°	1.00° × (0.33°-1.00°)
7	EC-Earth3-Veg	EC-Earth-Consortium/EU	0.70°×0.70°	1.00° × (0.33°-1.00°)
8	FGOALS-f3-L	CAS/China	1.25°×1.00°	1.00°×0.83°
9	GISS-E2-1-G-CC	NASA-GISS/USA	2.50°×2.00°	1.00°×1.00°
10	GISS-E2-1-G	NASA-GISS/USA	2.50°×2.00°	1.00°×1.00°
11	GISS-E2-1-H	NASA-GISS/USA	2.50°×2.00°	1.00°×1.00°
12	GISS-E2-2-G	NASA-GISS/USA	2.50°×2.00°	1.00°×1.00°
13	HadGEM3-GC31-LL	MOHC/UK	1.88°×1.25°	1.00° × (0.33°-1.00°)
14	HadGEM3-GC31-MM	MOHC/UK	0.83°×0.56°	0.25°×0.25°
15	INM-CM4-8	INM/Russia	2.00°×1.50°	1.00°×1.00°
16	INM-CM5-0	INM/Russia	2.00°×1.50°	1.00°×1.00°
17	IPSL-CM6A-LR	IPSL/France	2.50°×1.27°	1.00° × (0.33°-1.00°)
18	MCM-UA-1-0	UA/USA	3.75°×2.5°	1.88°×2.50°
19	MIROC6	MIROC/Japan	1.41°×1.40°	1.00°×1.00°
20	MPI-ESM1-1-2-HAM	HAMMOZ/Germany	1.88°×1.86°	1.50°×1.50°
21	MPI-ESM1-2-HR	MPI-M/Germany	0.94°×0.94°	0.40°×0.40°
22	MPI-ESM1-2-LR	MPI-M/Germany	1.88°×1.86°	1.50°×1.50°
23	MRI-ESM2-0	MRI/Japan	1.13°×1.13°	1.00°×0.50°
24	NESM3	NUIST/China	1.88°×1.86°	1.00°×1.00°
25	NorCPM1	NCC/Norway	1.41°×1.40°	1.00°×1.00°

Figures

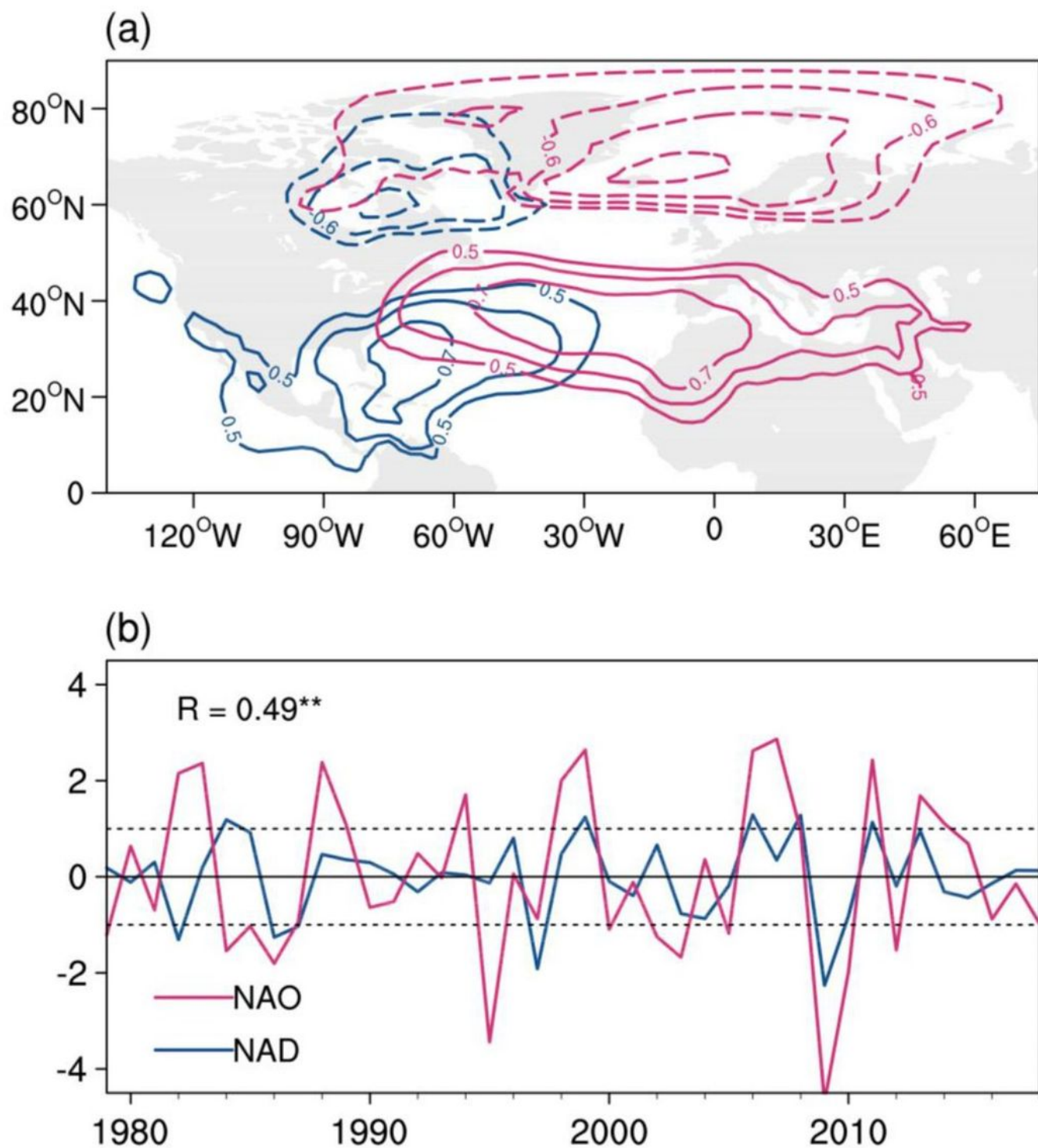


Figure 1

Please see the Manuscript PDF file for the complete figure caption Note: The designations employed and the presentation of the material on this map do not imply the expression of any opinion whatsoever on the part of Research Square concerning the legal status of any country, territory, city or area or of its

authorities, or concerning the delimitation of its frontiers or boundaries. This map has been provided by the authors.

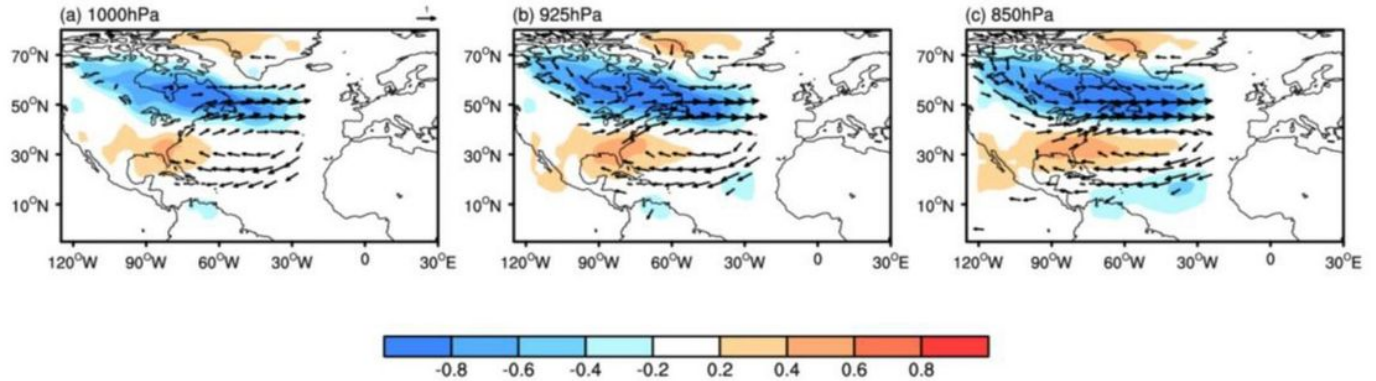


Figure 2

Please see the Manuscript PDF file for the complete figure caption Note: The designations employed and the presentation of the material on this map do not imply the expression of any opinion whatsoever on the part of Research Square concerning the legal status of any country, territory, city or area or of its authorities, or concerning the delimitation of its frontiers or boundaries. This map has been provided by the authors.

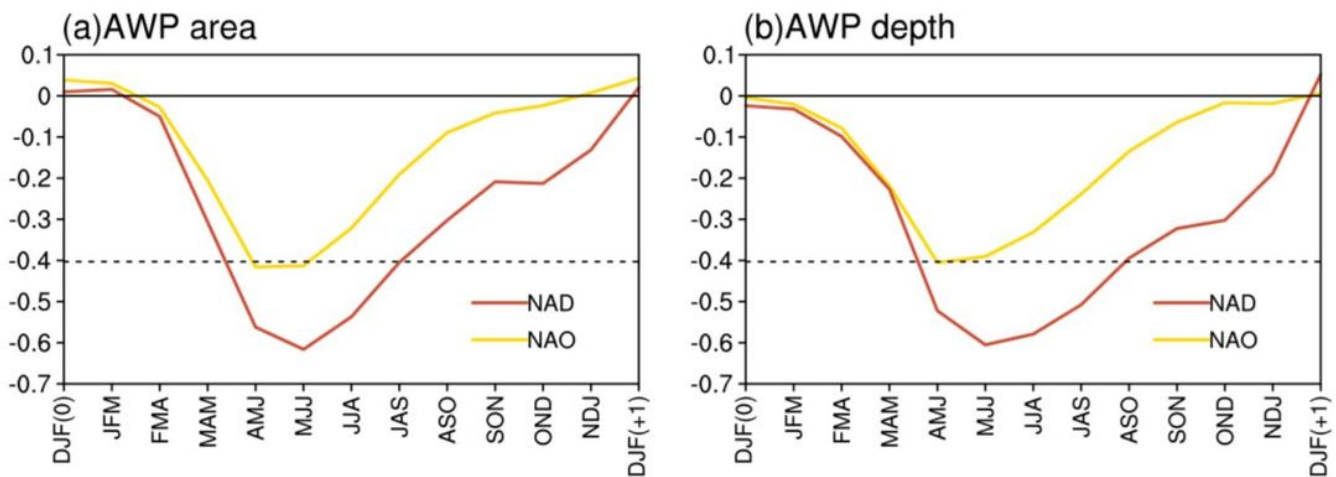


Figure 3

Please see the Manuscript PDF file for the complete figure caption

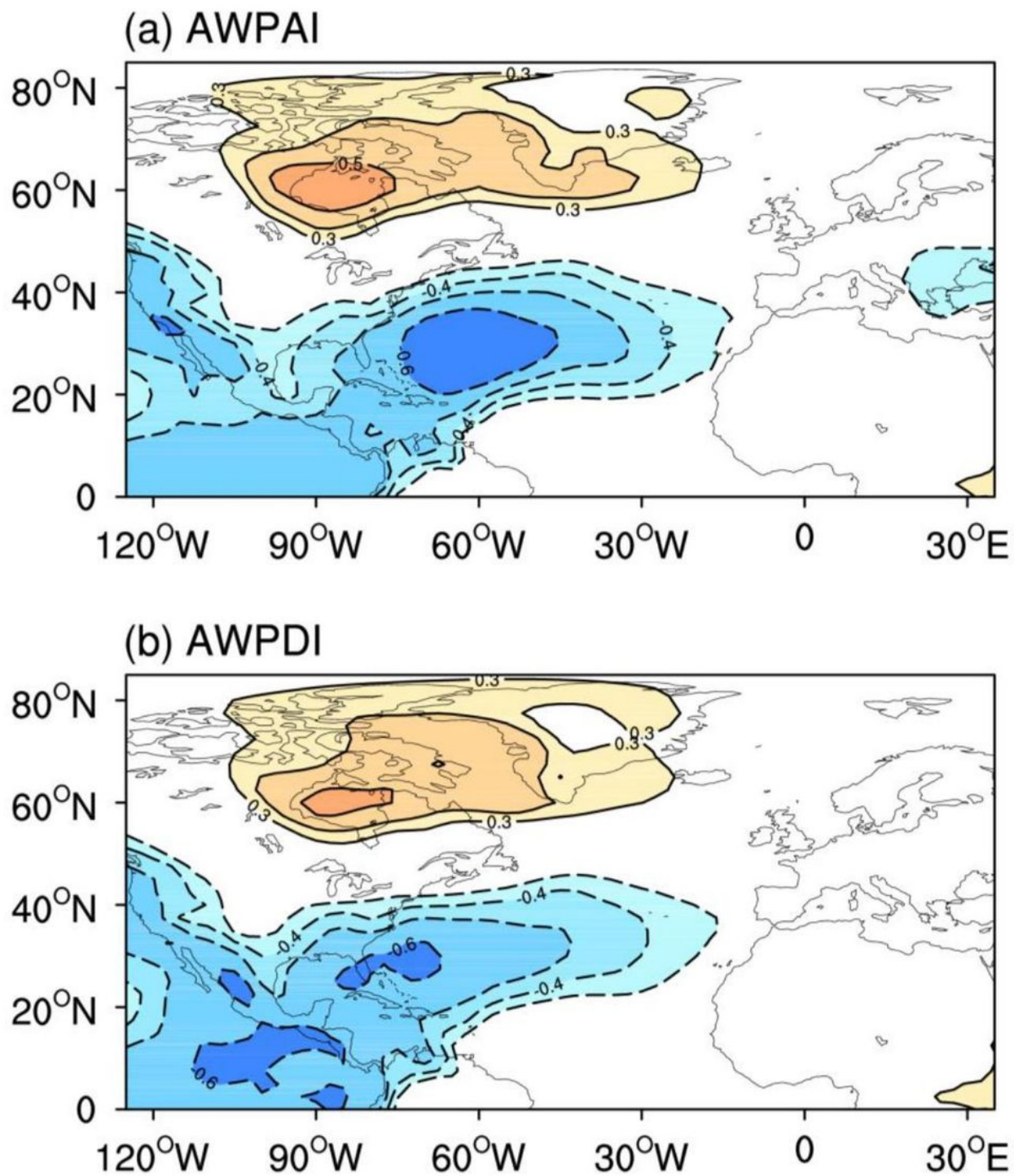


Figure 4

Please see the Manuscript PDF file for the complete figure caption Note: The designations employed and the presentation of the material on this map do not imply the expression of any opinion whatsoever on the part of Research Square concerning the legal status of any country, territory, city or area or of its authorities, or concerning the delimitation of its frontiers or boundaries. This map has been provided by the authors.

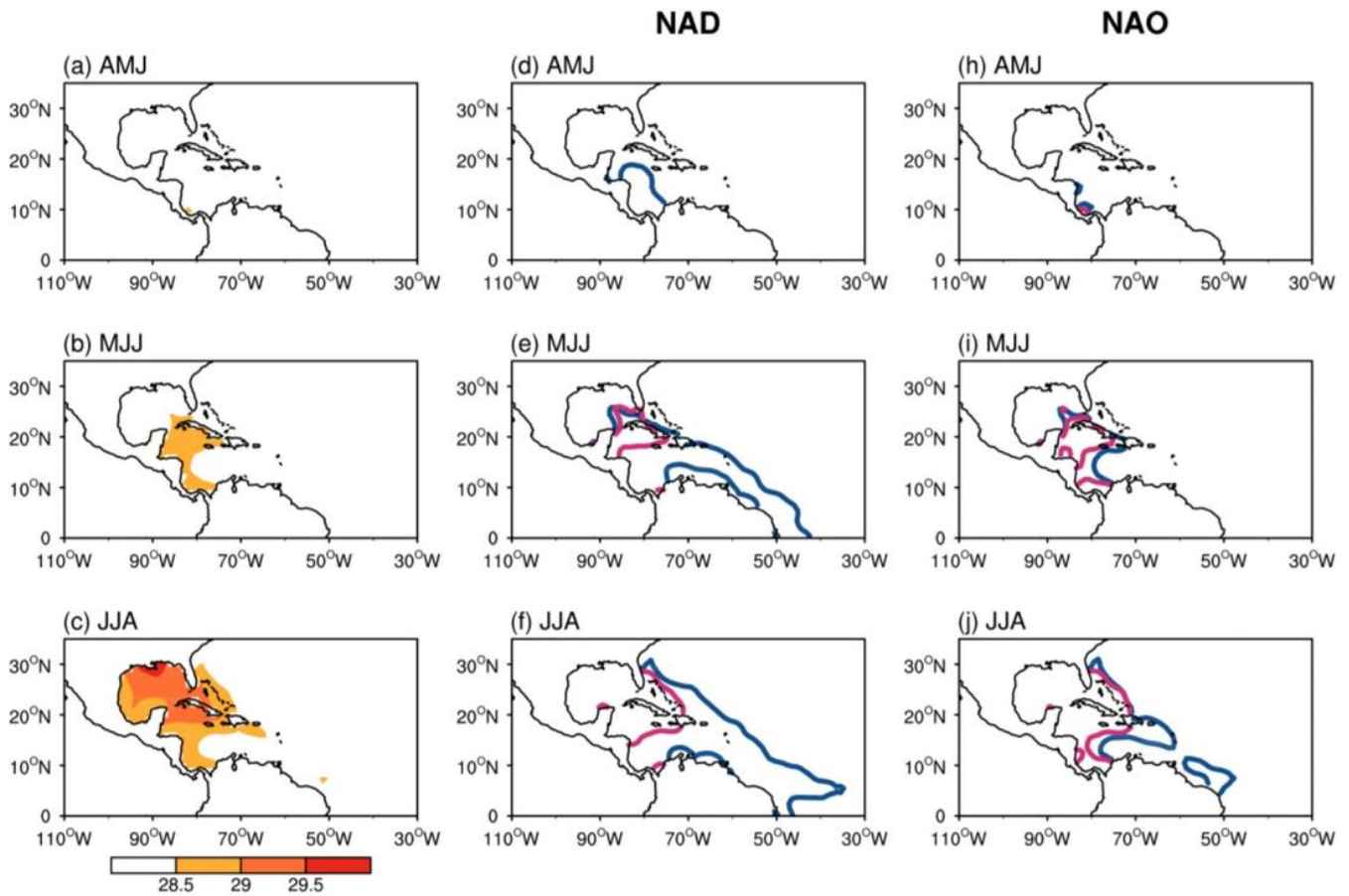


Figure 5

Please see the Manuscript PDF file for the complete figure caption Note: The designations employed and the presentation of the material on this map do not imply the expression of any opinion whatsoever on the part of Research Square concerning the legal status of any country, territory, city or area or of its authorities, or concerning the delimitation of its frontiers or boundaries. This map has been provided by the authors.

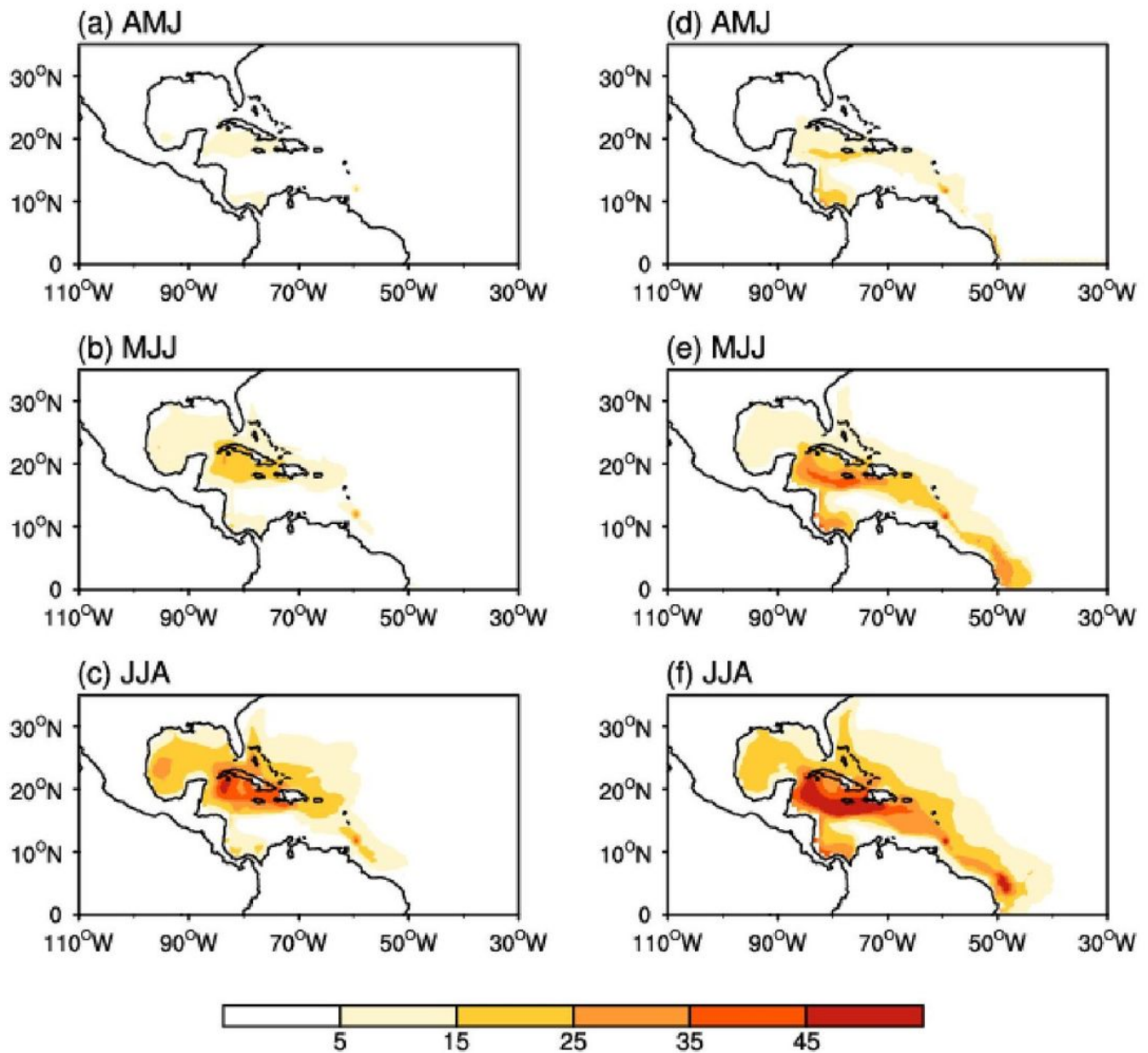


Figure 6

Please see the Manuscript PDF file for the complete figure caption Note: The designations employed and the presentation of the material on this map do not imply the expression of any opinion whatsoever on the part of Research Square concerning the legal status of any country, territory, city or area or of its authorities, or concerning the delimitation of its frontiers or boundaries. This map has been provided by the authors.

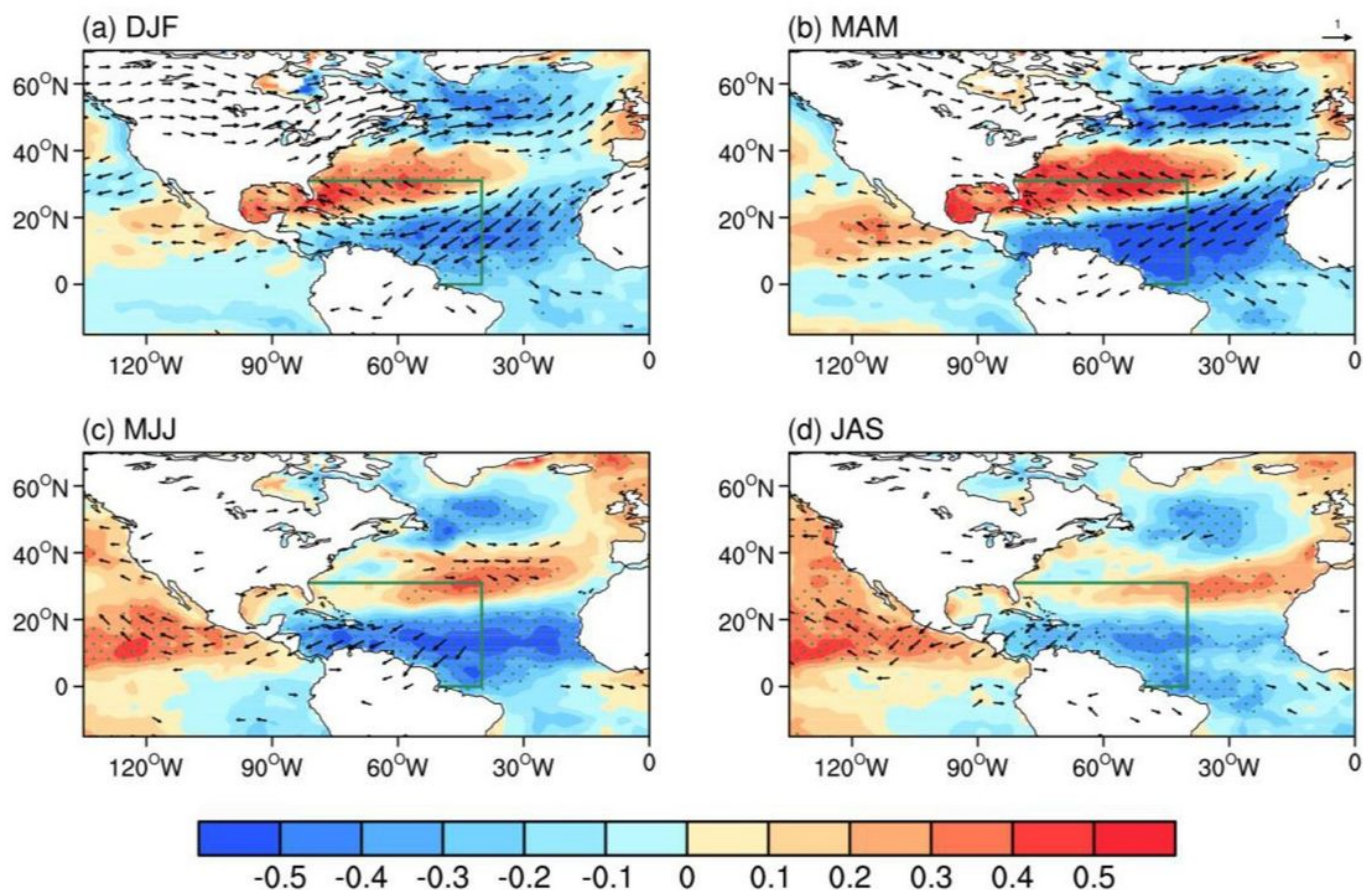


Figure 7

Please see the Manuscript PDF file for the complete figure caption Note: The designations employed and the presentation of the material on this map do not imply the expression of any opinion whatsoever on the part of Research Square concerning the legal status of any country, territory, city or area or of its authorities, or concerning the delimitation of its frontiers or boundaries. This map has been provided by the authors.

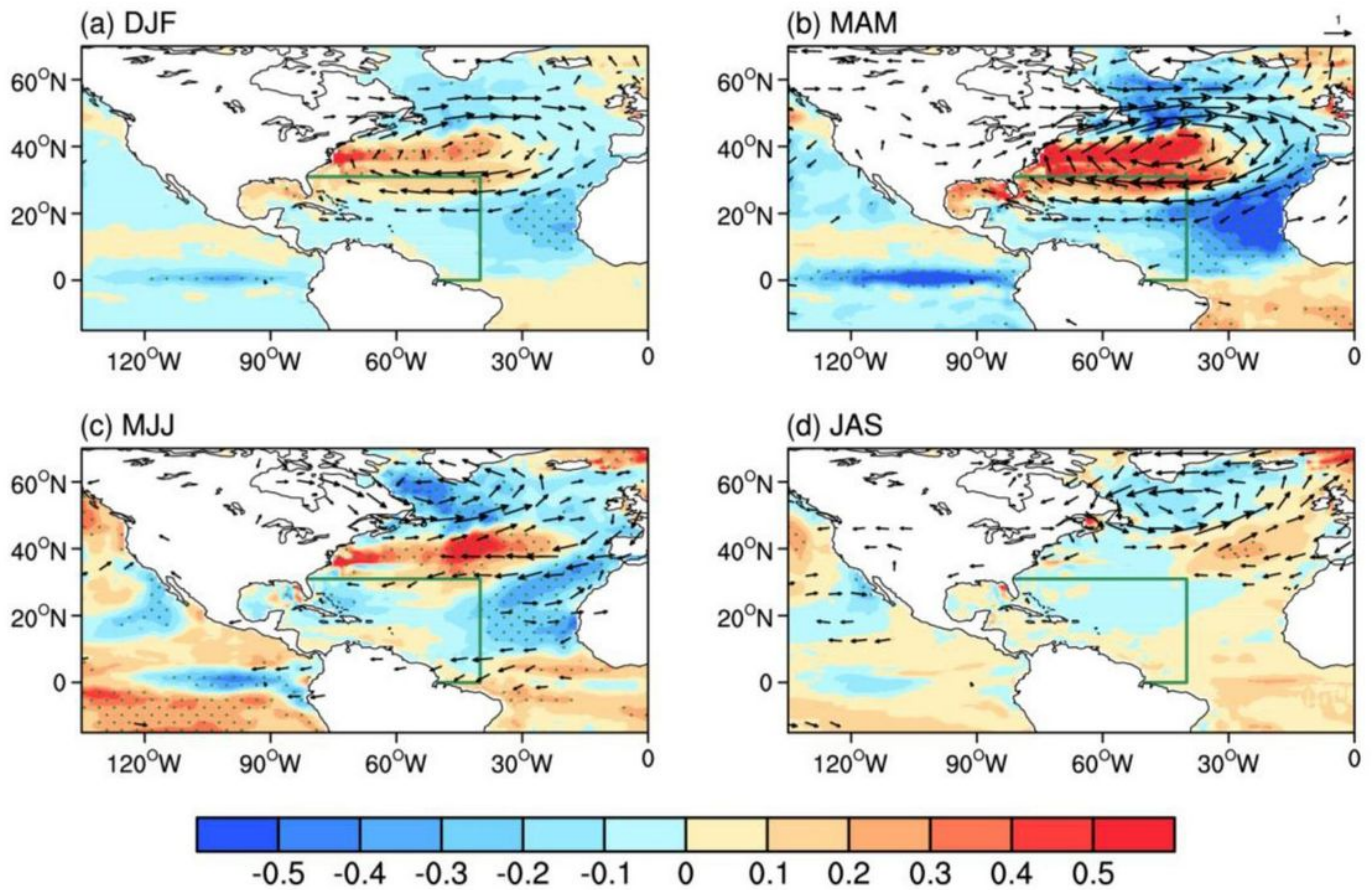


Figure 8

Please see the Manuscript PDF file for the complete figure caption Note: The designations employed and the presentation of the material on this map do not imply the expression of any opinion whatsoever on the part of Research Square concerning the legal status of any country, territory, city or area or of its authorities, or concerning the delimitation of its frontiers or boundaries. This map has been provided by the authors.

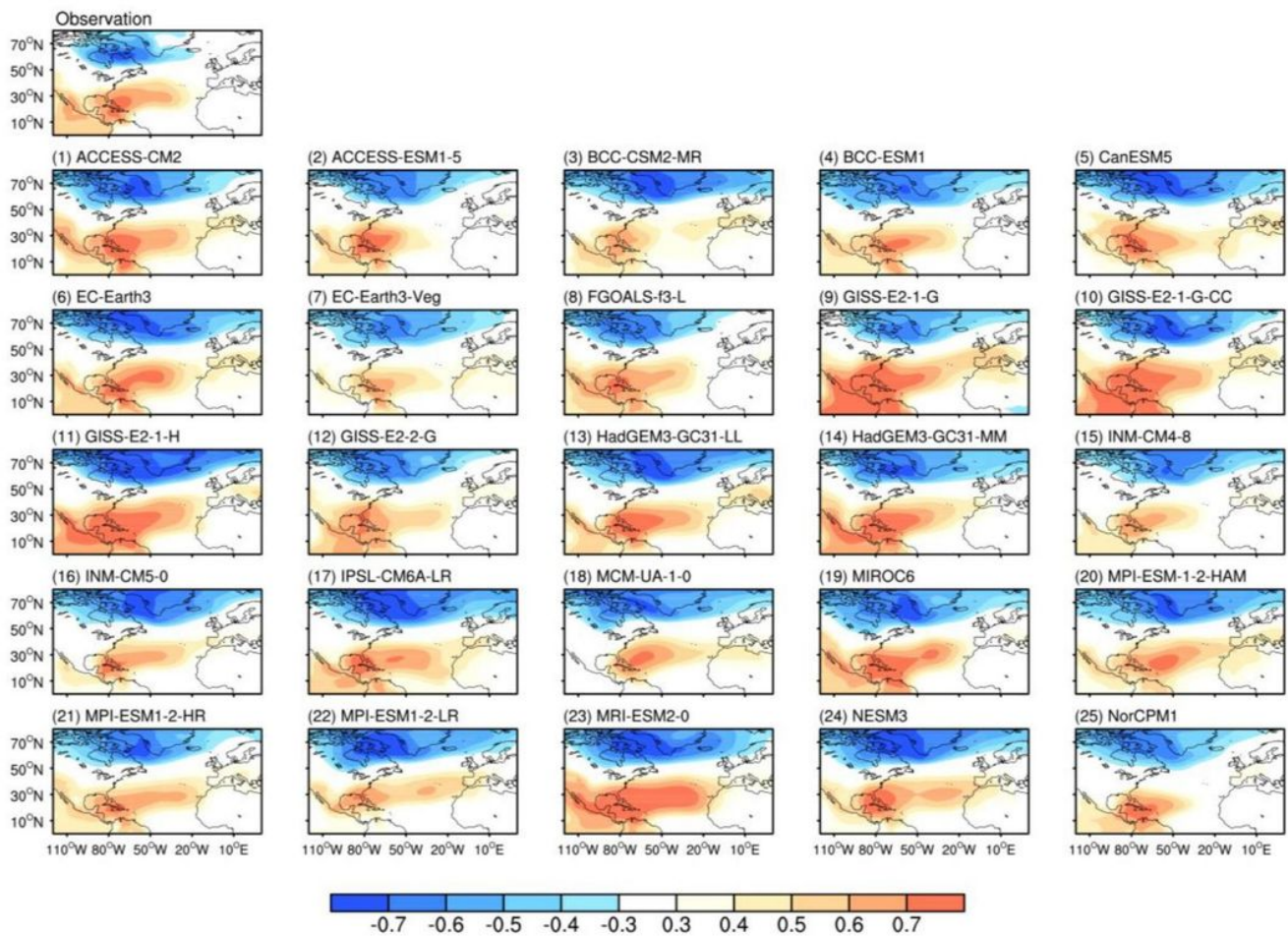


Figure 9

Please see the Manuscript PDF file for the complete figure caption Note: The designations employed and the presentation of the material on this map do not imply the expression of any opinion whatsoever on the part of Research Square concerning the legal status of any country, territory, city or area or of its authorities, or concerning the delimitation of its frontiers or boundaries. This map has been provided by the authors.

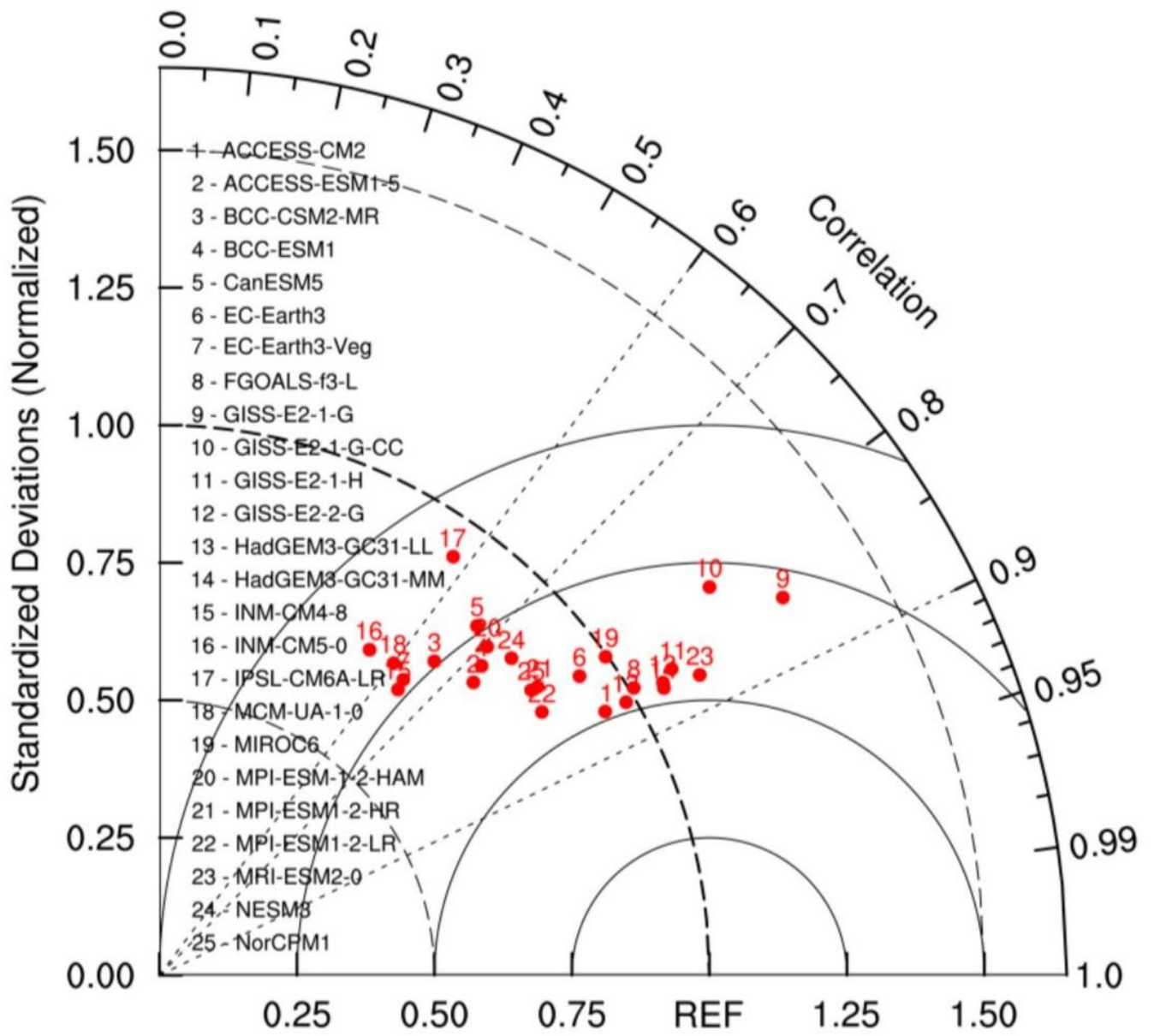


Figure 10

Please see the Manuscript PDF file for the complete figure caption

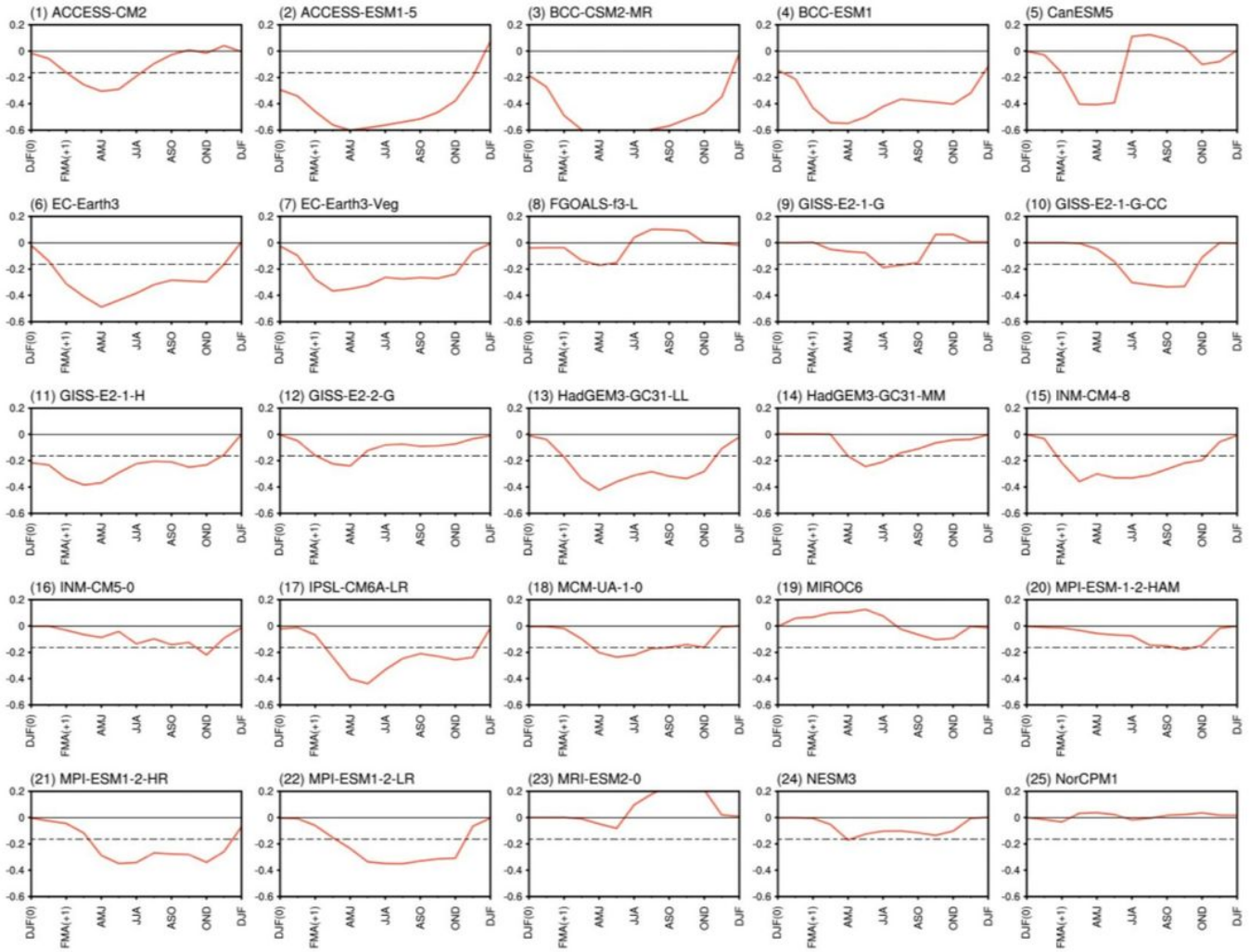


Figure 11

Please see the Manuscript PDF file for the complete figure caption

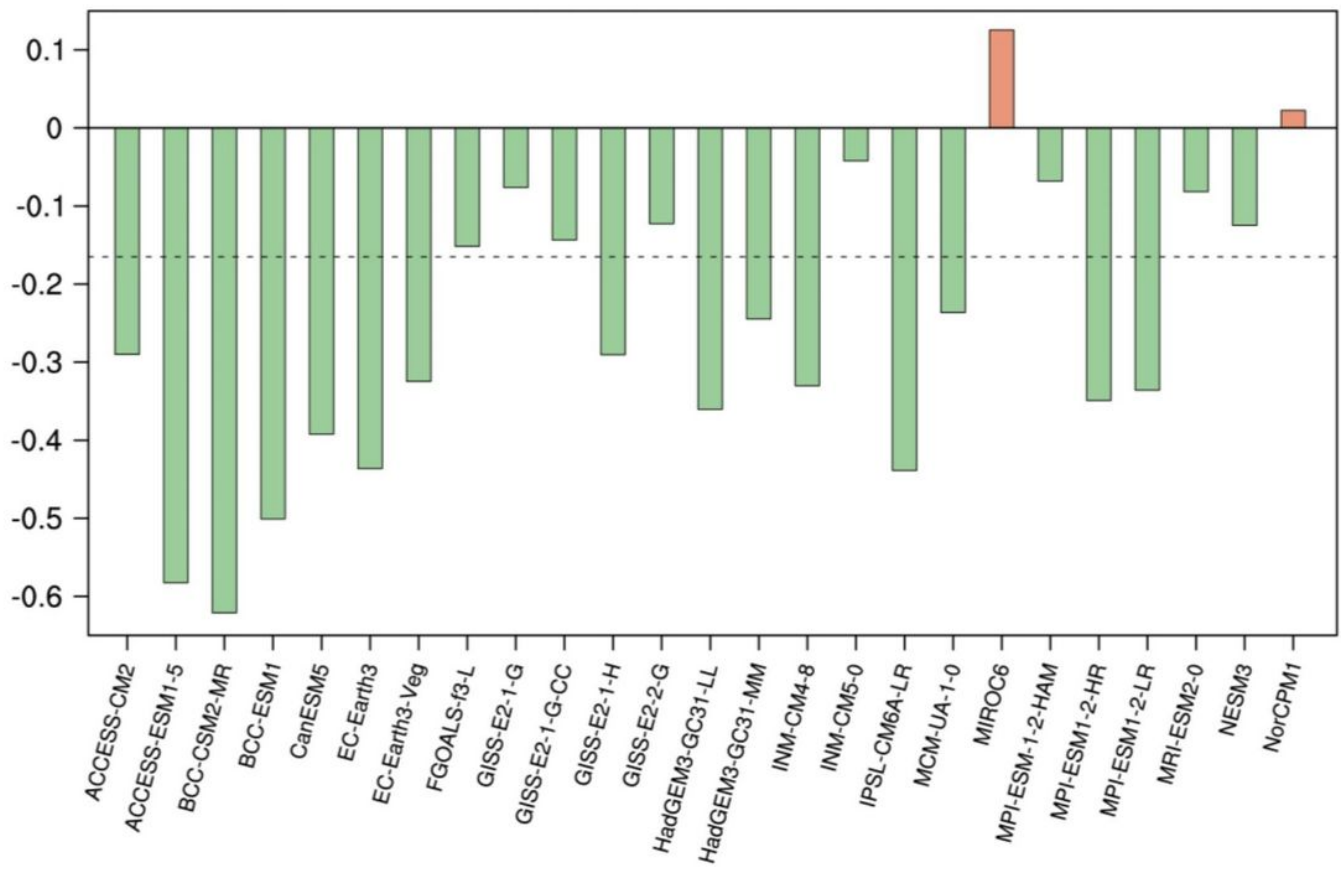


Figure 12

Please see the Manuscript PDF file for the complete figure caption

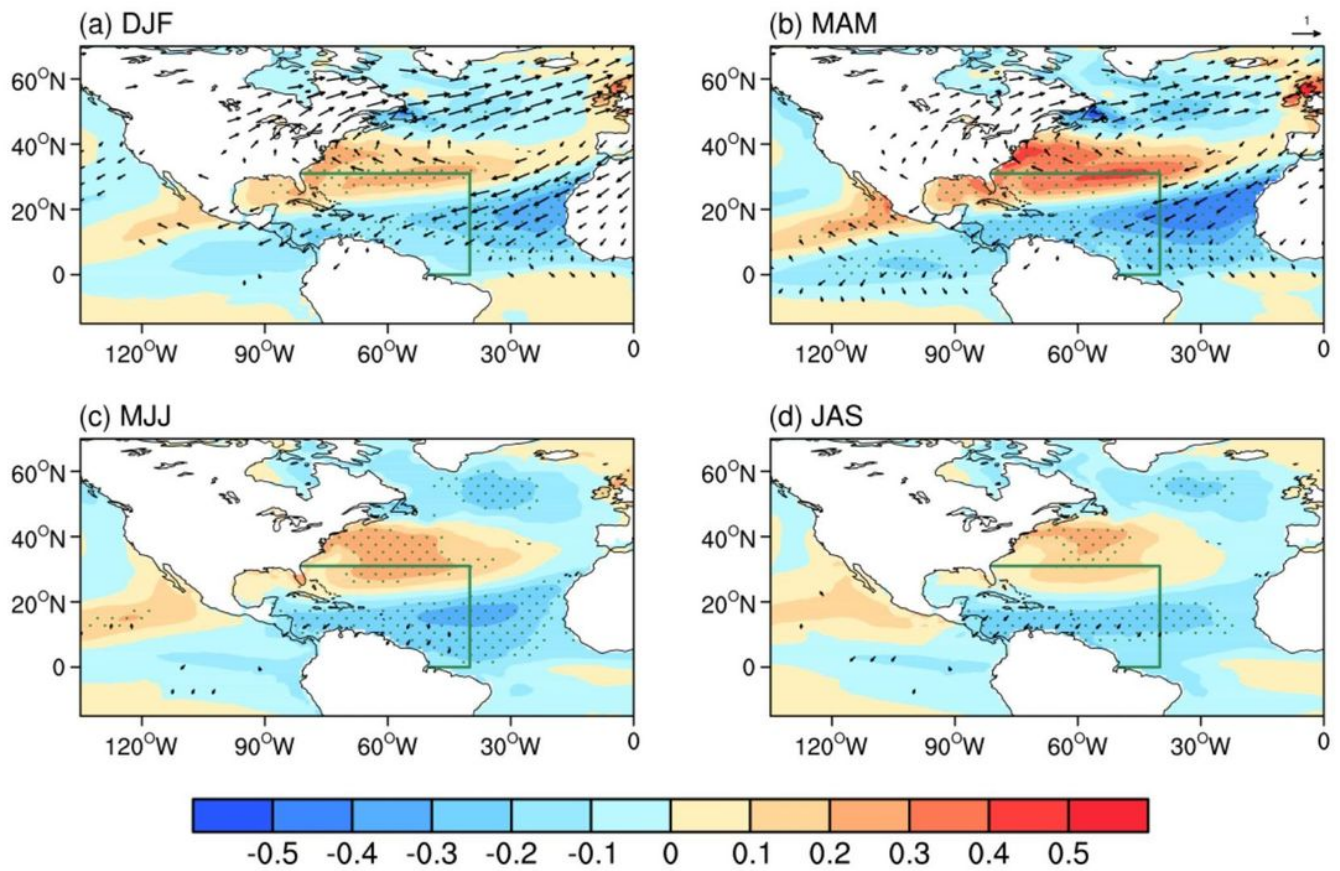


Figure 13

Please see the Manuscript PDF file for the complete figure caption Note: The designations employed and the presentation of the material on this map do not imply the expression of any opinion whatsoever on the part of Research Square concerning the legal status of any country, territory, city or area or of its authorities, or concerning the delimitation of its frontiers or boundaries. This map has been provided by the authors.

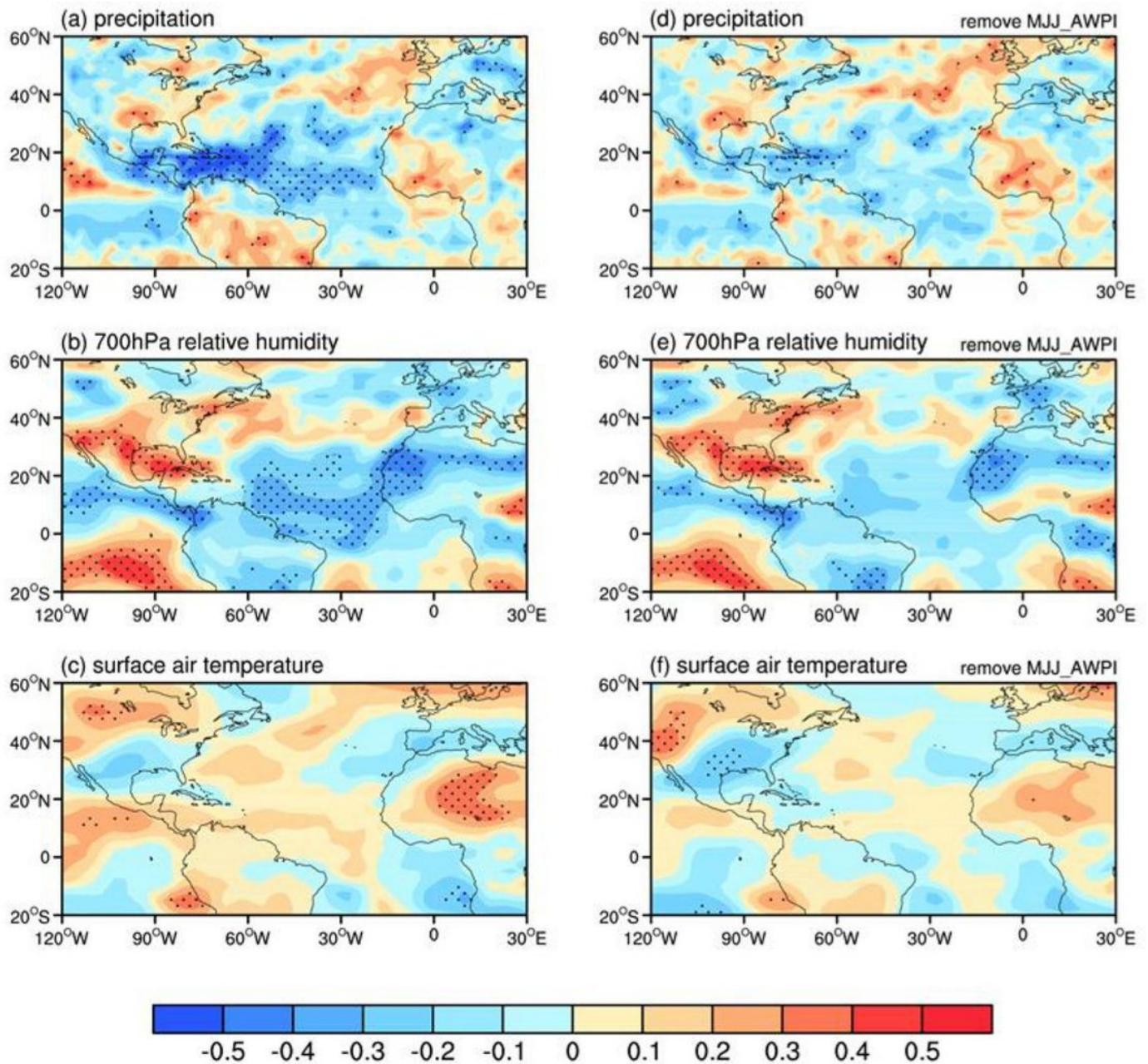


Figure 14

Please see the Manuscript PDF file for the complete figure caption Note: The designations employed and the presentation of the material on this map do not imply the expression of any opinion whatsoever on the part of Research Square concerning the legal status of any country, territory, city or area or of its authorities, or concerning the delimitation of its frontiers or boundaries. This map has been provided by the authors.

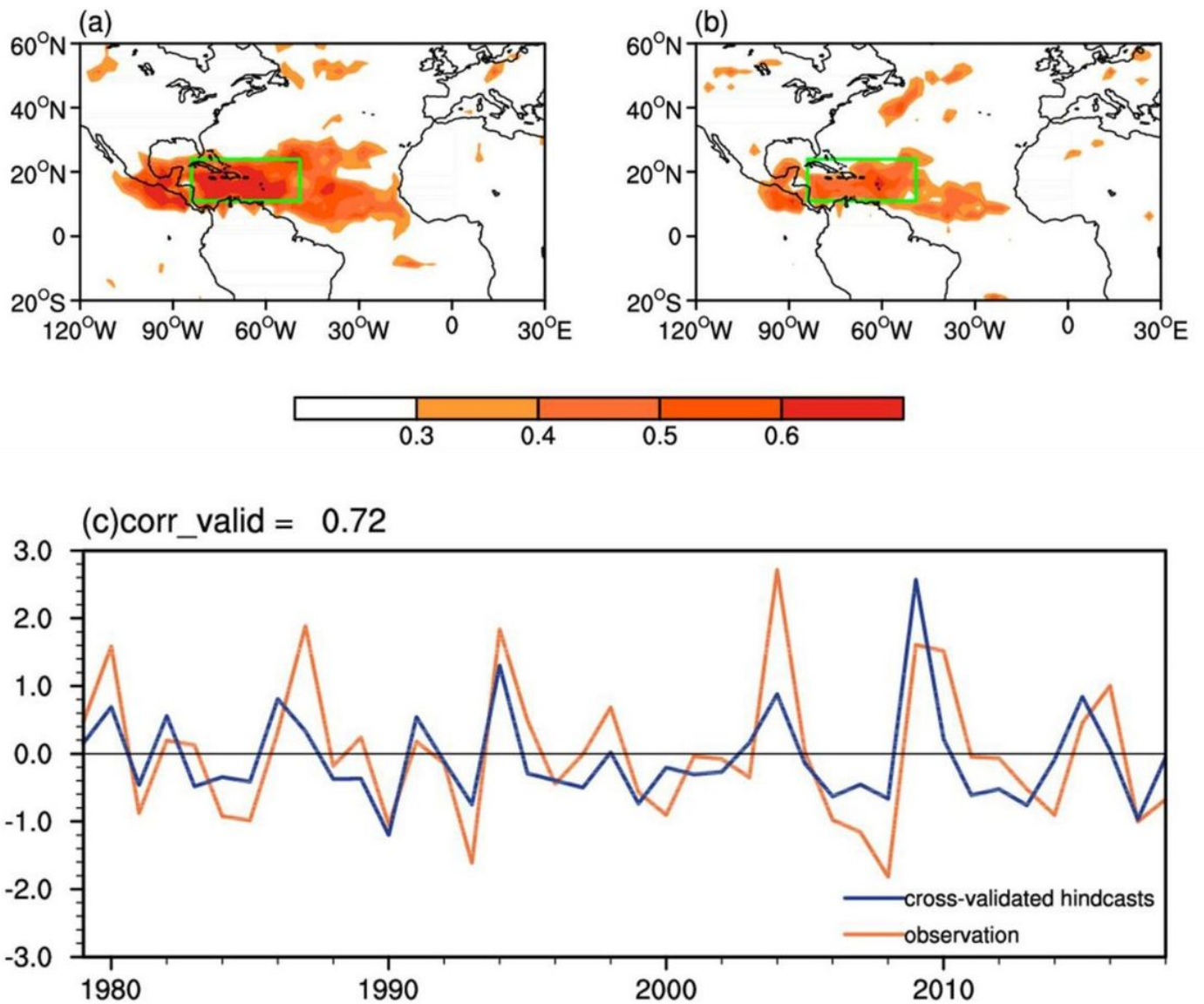


Figure 15

Please see the Manuscript PDF file for the complete figure caption Note: The designations employed and the presentation of the material on this map do not imply the expression of any opinion whatsoever on the part of Research Square concerning the legal status of any country, territory, city or area or of its authorities, or concerning the delimitation of its frontiers or boundaries. This map has been provided by the authors.